Delft University of Technology

Document Version
Final published version

Licence
CC BY

Citation (APA)
Rákóczi, H., Root, B. C., Messenger, C., & Hammond, G. (2026). Characterizing Martian Lithospheric Density Distribution Through Bayesian Gravity Analysis. *Journal of Geophysical Research: Planets*, *131*(7), Article e2026JE009757. https://doi.org/10.1029/2026JE009757

Important note
To cite this publication, please use the final published version (if applicable).
Please check the document version above.

Copyright
In case the licence states “Dutch Copyright Act (Article 25fa)”, this publication was made available Green Open Access via the TU Delft Institutional Repository pursuant to Dutch Copyright Act (Article 25fa, the Taverne amendment). This provision does not affect copyright ownership.
Unless copyright is transferred by contract or statute, it remains with the copyright holder.

Sharing and reuse
Other than for strictly personal use, it is not permitted to download, forward or distribute the text or part of it, without the consent of the author(s) and/or copyright holder(s), unless the work is under an open content license such as Creative Commons.

Takedown policy
Please contact us and provide details if you believe this document breaches copyrights.
We will remove access to the work immediately and investigate your claim.

This work is downloaded from Delft University of Technology.

Check for updates

JGR Planets

RESEARCH ARTICLE
10.1029/2026JE009757

Characterizing Martian Lithospheric Density Distribution Through Bayesian Gravity Analysis

Henrietta Rákóczi[1], **B. C. Root**[2], **Christopher Messenger**[1], **and Giles Hammond**[1]

[1]Institute for Gravitational Research, Physics and Astronomy, University of Glasgow, Glasgow, UK, [2]Planetary Exploration, Space Engineering, Delft University of Technology, Delft, The Netherlands

Key Points:

- Physically viable Martian lithospheric density structures are simulated using a Matérn covariance function
- Information about the lateral density distribution in the lithosphere is inferred using a Bayesian machine-learning inference technique
- The results indicate a spatially smooth density structure in the mantle, with more small-scale variations apparent in the crust

Supporting Information:

Supporting Information may be found in the online version of this article.

Correspondence to:

H. Rákóczi,
rakoczi.henrietta@proton.me

Citation:

Rákóczi, H., Root, B. C., Messenger, C., & Hammond, G. (2026). Characterizing Martian lithospheric density distribution through Bayesian gravity analysis. *Journal of Geophysical Research: Planets*, *131*, e2026JE009757. https://doi.org/10.1029/2026JE009757

Received 20 FEB 2026
Accepted 10 JUL 2026

Author Contributions:

Conceptualization: Henrietta Rákóczi, B. C. Root, Christopher Messenger
Formal analysis: Henrietta Rákóczi
Funding acquisition: Giles Hammond
Investigation: Henrietta Rákóczi
Methodology: Henrietta Rákóczi
Resources: B. C. Root
Software: Henrietta Rákóczi
Supervision: Christopher Messenger, Giles Hammond
Validation: Henrietta Rákóczi, B. C. Root, Christopher Messenger
Visualization: Henrietta Rákóczi
Writing – original draft: Henrietta Rákóczi

© 2026 The Author(s). Journal of Geophysical Research: Planets published by Wiley Periodicals LLC on behalf of American Geophysical Union.
This is an open access article under the terms of the Creative Commons Attribution License, which permits use, distribution and reproduction in any medium, provided the original work is properly cited.

Abstract One of the best sources of information for probing the inner structure of Mars is gravimetry data from satellites. By combining these measurements with topography data and isostatic theory, the aim of this study is to infer information about lateral density variations in the Martian lithosphere. Previous efforts at direct gravity inversion had limited success due to inherent degeneracies between the gravitational effects of different planetary layers. This study takes a different approach, where the aim is not to obtain spatial density maps, but rather to gain information about the spatial distribution of density values. The density distributions are simulated via multivariate Gaussian sampling using a Matérn covariance function. Constraints on the Matérn parameters for Mars are obtained through Bayesian inference, which can inform about the sensitivity of gravity data to different aspects of the density distribution and can be translated into physically meaningful insights about the lithospheric structure. The inference is performed with a machine-learning technique, namely Normalizing Flows. The results of this study are consistent with previous findings and indicate that the upper mantle exhibits significantly smoother density variations than the crust, with both layers containing large, connected regions with similar densities.

Plain Language Summary Gravimetry data from satellites provide a window into the interior of Mars, conveying information about density variations within the planet. However, gravimetry alone does not resolve how density varies with depth, therefore, constructing a three-dimensional model of the Martian density structure remains challenging. Rather than producing spatial density maps of individual planetary layers, we aim to infer the statistical characteristics of density variations within these layers. We simulate artificial planets consisting of three layers that broadly resemble the structure of Mars but contain randomized density distributions. The parameterization of these distributions allows us to interpret various characteristics of the density structure. We conduct the analysis using a machine-learning technique that also provides estimates of uncertainties on the inferred parameter values. Our results show that the Martian crust is characterized by density variations over small spatial scales, while the mantle has a smoother density distribution and both layers are likely to contain large, connected regions with similar average densities. Our findings are consistent and complementary to previous interpretations of the Martian interior, while introducing a novel approach to the analysis of satellite gravimetry data. Our results can be directly incorporated in future studies aiming to produce spatial density maps.

1. Introduction

Mars is the fourth planet from the Sun and the second smallest planet in the Solar System. It has a similar structure to Earth, in that it is a terrestrial planet made up of a core, a mantle and a crust with different material properties. The inner structure of Mars is widely studied in the literature, for instance via thermal modeling (Guinard et al., 2025; Plesa et al., 2018), the analysis of topography and gravity data (Belleguic et al., 2005; Beuthe et al., 2012; Goossens et al., 2017; Liang et al., 2022; G. A. Neumann et al., 2004; Nimmo & Stevenson, 2001; Pauer & Breuer, 2008; M. T. Zuber et al., 2000) and more recently via the analysis of seismic (Coulson et al., 2007; Drilleau et al., 2023; Khan et al., 2021; Kim et al., 2023; Knapmeyer-Endrun et al., 2021; Samuel et al., 2023; Shi et al., 2023; Stähler et al., 2021) and magnetometry (Mittelholz et al., 2023) measurements from the InSight lander located in the Elysium region. To further constrain the mineral composition of the planet, meteorites originating from Mars provide samples of surface rock (Coulson et al., 2007).

Stähler et al. (2021) inverted geodetic and seismic data to find that Mars likely has a large liquid metal core, and consequently lacks a lower mantle, with only a single rocky upper-mantle layer that is mineralogically similar to

Writing – review & editing: B. C. Root, Christopher Messenger, Giles Hammond

that of Earth. In an alternative model, suggested by Samuel et al. (2023), the mantle contains a thin molten silicate layer directly above the core. Also from seismic data, the crust was shown to likely have at least three (Knapmeyer-Endrun et al., 2021), but potentially four layers (Drilleau et al., 2023; Shi et al., 2023) beneath the Elysium region. The global average thickness of the crust was inferred via the analysis of seismic data (Kim et al., 2023; Knapmeyer-Endrun et al., 2021), from gravity and topography data (G. A. Neumann et al., 2004), and all these sources combined (M. A. Wieczorek et al., 2022). While the InSight lander provides local data from the surface, the two sources of data with global coverage originate from satellite measurements of the gravitational field (Konopliv et al., 2016) and surface topography (Smith et al., 2001). Satellite gravimetry data has been used to constrain the density (Belleguic et al., 2005; Goossens et al., 2017; Pauer & Breuer, 2008), structure (G. A. Neumann et al., 2004; M. T. Zuber et al., 2000) and elastic thickness (Beuthe et al., 2012) of the lithosphere. The first attempt at the combined inversion of seismological, geodetic, gravity and topography data provided constraints on the lateral variations of crustal thickness and two possible scenarios for the thermal evolution of Mars (Drilleau et al., 2024).

This study focuses on Mars's outermost layer, the lithosphere, which consists of the crust and the upper mantle. The Martian lithosphere differs from that of Earth, as it can support much larger surface loads, evidenced by the Solar System's largest volcano, Olympus Mons (Taylor et al., 2020). Obtaining a global density map of the Martian lithosphere is highly desirable. However, relying only on gravimetry and topography data poses challenges due to non-uniqueness and degeneracies, and other types of global geophysical data are currently unavailable. The existing planetary models contain too many unknowns to allow for a unique solution or to construct a definitive density map of the two or more lithospheric layers. Therefore, previous attempts at global gravity inversion had limited success (Phillips et al., 1973; van Brummen, 2022). This work aims to aid gravity inversion methods by inferring information about the standard deviation (SD), spatial correlation and smoothness of the density distributions in the crust and the mantle from gravimetry data.

In this work, we study the parameters describing the distribution of Mars's lithospheric density structure using Bayesian inference (Bayes, 1763) from satellite gravimetry and topography data. We constructed planetary models to approximate the Martian density structure, where we assumed that the density distributions in Mars's crust and mantle can be simulated using multivariate normal distributions with a Matérn covariance function (Gneiting et al., 2010). The goal of this study is to understand the parameters that define these covariance functions, as they govern the distributions of the densities. Due to limitations of standard techniques in this context, we used a likelihood-free machine learning approach to perform the inference. Our machine learning method is physics-informed in that the training data set encodes known features of the Martian planetary interior and draws on observed data and theoretical frameworks such as isostasy theory and the mathematical form of planetary gravitational fields.

2. Input Data

The current most accurate and high-resolution information of Mars's surface topography comes from the measurements taken by the Mars Orbital Laser Altimeter (MOLA) (Smith et al., 2001) taken over 4 years (1997–2001) on board the Mars Global Surveyor (MGS) mission. The topography data is available on the PDS Geosciences Node (G. Neumann et al., 2003) in a range of resolutions. The elevation profile is defined relative to the areoid, a model of which is also available on the PDS Geosciences Node. The data used in this study is shown in Figure 1a. The topography data was down-sampled by computing the mean value over each $4° \times 4°$ region, equivalent to 236 km × 236 km on Mars.

Measurements of the gravitational field can be obtained from radio tracking data from satellites orbiting Mars. Both the Goddard Mars Model-3 (GMM-3) (Genova et al., 2016) and the MRO120 data sets are available on the PDS Geosciences Node (M. Zuber et al., 2010) in spherical harmonic (SH) format. We applied the MRO120F data set here, which uses the Mars Reconnaissance Orbiter (MRO) as its main data source, but also includes data from a number of other instruments; MGS, Mars Odyssey, Pathfinder, Viking Lander and MER Opportunity, and uses power-law approximations from Kaula's rule to constrain the gravity spectrum at high degrees (Konopliv et al., 2016). The spatial resolution of $4° \times 4°$ used in the analysis corresponds to a maximum SH degree of $n = 45$. Therefore, the gravity spectra were considered only up to this degree. The low SH degrees in the gravity spectrum are sensitive to large-scale features in the planet's structure, such as polar flattening and deep mantle anomalies. According to Belleguic et al. (2005), the first 6 SH degrees of the gravity spectrum are dominated by

21699100, 2026, 7, Downloaded from https://agupubs.onlinelibrary.wiley.com/doi/10.1029/2026JE009757 by Technical University Delft, Wiley Online Library on [30/07/2026]. See the Terms and Conditions (https://onlinelibrary.wiley.com/terms-and-conditions) on Wiley Online Library for rules of use; OA articles are governed by the applicable Creative Commons License

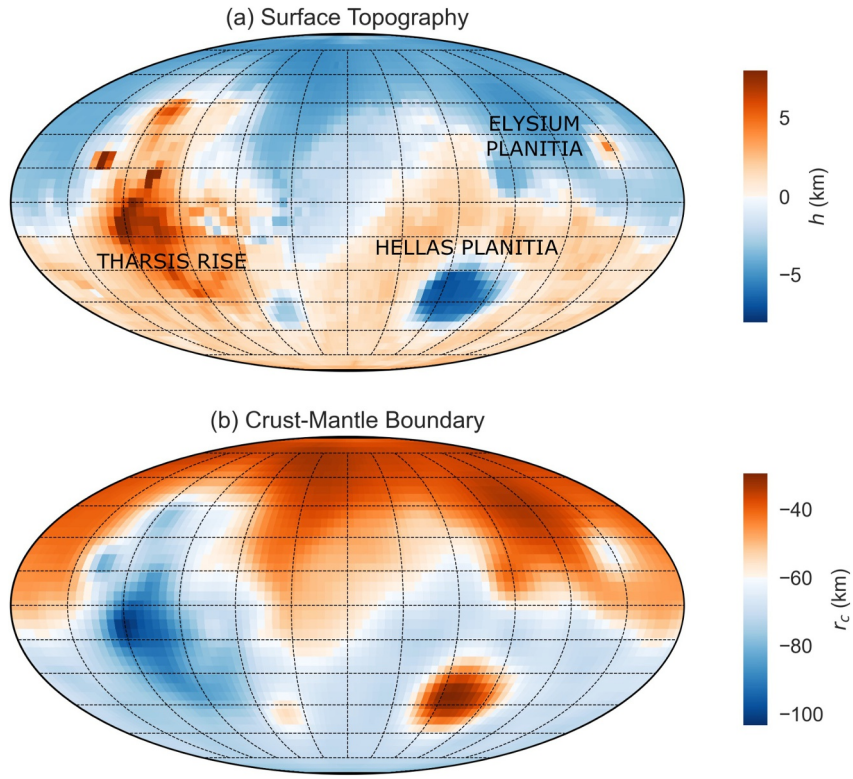

Figure 1. (a) A map of the global surface topography of Mars, relative to the areoid. The data was obtained from the PDS Geosciences Node (G. Neumann et al., 2003) and downsampled to 4° × 4° resolution. While the true maximum elevation reaches ∼21 km, the color range was truncated for better visibility. (b) The elevation map of the crust-mantle boundary modeled from the surface topography of Mars.

the Tharsis Rise, and Beuthe et al. (2012) extends this assumption to the first 7°. In addition, the hypothesized mantle plume beneath Elysium Planitia (Broquet & Andrews-Hanna, 2022) (∼4,000 km diameter) would be expected to increase the power at low degrees. Root et al. (2026) finds that the power spectrum is dominated by mantle flow at $n < 8$. Since these features are not the focus of this study and were not included in the planetary simulations, the gravity spectra were reduced to exclude $n < 7$.

3. Simulation of the Planetary Gravitational Field

Using global spherical harmonic synthesis (GSHS), or *gravity synthesis*, we can express the radial component of the gravitational acceleration (M. Wieczorek, 2015) in terms of spherical coordinates $\boldsymbol{R} = (\omega', \lambda', \phi)$, where ω' is the radial distance from the center of the object, as

$$g_r(\boldsymbol{R}) = \frac{GM}{\omega'^2} \sum_{n=0}^{\infty} \sum_{m=-n}^{n} \left(\frac{R_0}{\omega'}\right)^n (n+1) c_{nm} Y_{nm}. \quad (1)$$

In this study, we use the convention that the gravitational acceleration values are positive when pointing toward the center of the sphere. In the expression above, $G = 6.6743 \times 10^{-11}$ m^3 kg^{-1} s^{-2} is the gravitational constant (Kaula, 1966; M. Wieczorek, 2015) and, in case of Mars, the mass of the object is $M = M_{\mathcal{O}} = 6.4171 \times 10^{24}$ kg and the reference radius is $R_0 = R_{\mathcal{O}} = 3{,}396$ km. In reality, we do not compute the sum to infinity but to a maximum degree $N = 45$, which is chosen based on the requirements of the analysis and considerations of computational cost. The SH functions are defined as

21699100, 2026, 7, Downloaded from https://agupubs.onlinelibrary.wiley.com/doi/10.1029/2026JE009757 by Technical University Delft, Wiley Online Library on [30/07/2026]. See the Terms and Conditions (https://onlinelibrary.wiley.com/terms-and-conditions) on Wiley Online Library for rules of use; OA articles are governed by the applicable Creative Commons License

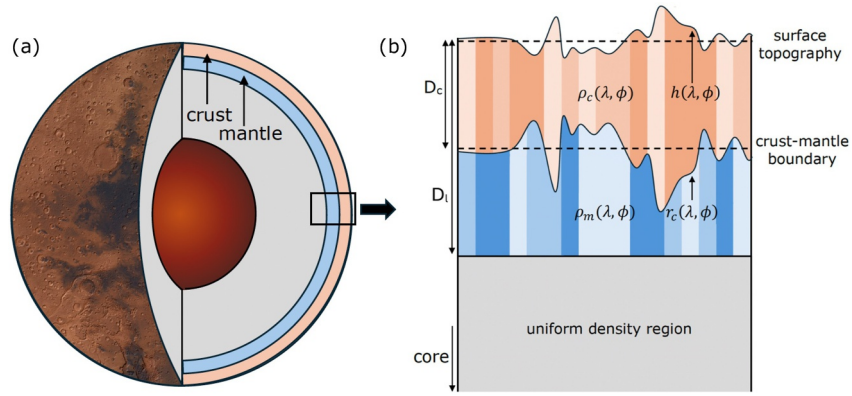

Figure 2. Diagram of the structure of Mars used in the simulated planetary models in this work. (a) A 3-dimensional sliced view of the planet, showing the outer two layers and the uniform density interior and core. (b) The zoomed-in version of the rectangle marked in (a). This is a 2-dimensional slice of the planetary layers, which can be extended into a 3-dimensional model of the planet. Both the crust and the mantle are modeled as shells of material consisting of columns of varying densities defined by the distributions $\rho_c(\lambda,\phi)$ and $\rho_m(\lambda,\phi)$, respectively. The surface topography and the crust-mantle boundary are defined as 2-dimensional maps of elevation. The average depth of the crust-mantle boundary is the compensation depth D_c and the depth to the bottom of the lithosphere is D_l.

$$Y_{nm}(\lambda,\phi) = \begin{cases} \overline{P}_{nm}(\cos\lambda)\cos m\phi & m \geq 0 \\ \overline{P}_{nm}(\cos\lambda)\sin|m|\phi & m < 0 \end{cases}, \tag{2}$$

where $\overline{P}_{nm}$ are the normalized Legendre functions, n is the degree and m is the order of these functions. The SH coefficients, c_{nm}, are unitless quantities. Using global spherical harmonic analysis (GSHA), or *gravity analysis*, c_{nm} can be expressed as

$$c_{nm} = \frac{1}{MR_o^n(2n+1)}\int_V \rho(\boldsymbol{r})\omega^n Y_{nm}(\lambda,\phi)dv, \tag{3}$$

where $\rho(\boldsymbol{r})$ is the density distribution within the object defined in the spherical domain, $\boldsymbol{r} = (\omega,\lambda,\phi)$. The integral is evaluated over V, the domain in which the source model is defined, and $dv = d\omega d\lambda d\phi$. The SH coefficients with positive ($m \geq 0$) and negative order ($m < 0$) are conventionally referred to as C_{nm} and S_{nm}, respectively. The *degree variance* (unitless) of the SH coefficients can be defined as

$$\mathcal{P}(n) = \sum_{m=0}^{n} C_{nm}^2 + S_{nm}^2, \tag{4}$$

which we use throughout this study to interpret and visualize data in the spectral domain.

The method described in this section is the forward model that links the planetary model (Section 4), defined by $\rho(\boldsymbol{r})$, to the gravitational field. We applied a fast spectral method for gravity synthesis and analysis for terrestrial planets made up of layers of materials with different properties (Root et al., 2016) using the `GSH` Matlab package (Root, 2021).

4. The Planetary Models

For this analysis, we require planetary models that approximate the structure of Mars in aspects that affect the measured gravitational field. Therefore, the planet is modeled in terms of its density structure, both laterally and radially. A diagram of the planetary model used in this study is shown in Figure 2, which consists of three planetary layers; the crust, mantle and the rest of the interior. In the model, we defined these layers by the depth and elevation profile (topography) of the boundaries separating them and by their lateral density distributions. We

21699100, 2026, 7, Downloaded from https://agupubs.onlinelibrary.wiley.com/doi/10.1029/2026JE009757 by Technical University Delft, Wiley Online Library on [30/07/2026]. See the Terms and Conditions (https://onlinelibrary.wiley.com/terms-and-conditions) on Wiley Online Library for rules of use; OA articles are governed by the applicable Creative Commons License

21699100, 2026, 7, Downloaded from https://agupubs.onlinelibrary.wiley.com/doi/10.1029/2026JE009757 by Technical University Delft, Wiley Online Library on [30/07/2026]. See the Terms and Conditions (https://onlinelibrary.wiley.com/terms-and-conditions) on Wiley Online Library for rules of use; OA articles are governed by the applicable Creative Commons License

assumed that the density below the lithosphere is uniform, shown in gray on the diagram, which has no effect on relative gravity measurements. The crust and the mantle were attributed density distributions with lateral variations defined by the functions $\rho_c(\lambda,\phi)$ and $\rho_m(\lambda,\phi)$, respectively, where λ is the longitude and ϕ is the latitude. Although the diagram presents only a 2-dimensional cross-section of the outer layers, the planetary model itself is 3-dimensional. Therefore, the crust and mantle are both thin spherical shells, each made up of vertical columns of material with uniform density, with the density variations from one column to another described by $\rho_c(\lambda,\phi)$ and $\rho_m(\lambda,\phi)$. The characteristics of these density distributions are the focus of this study, and the parameters defining them are the desired outputs of the inference. We assumed the mean values of the densities in the crust and the mantle to be $\overline{\rho}_c = 3{,}050$ kg/m^3 and $\overline{\rho}_m = 3{,}550$ kg/m^3, respectively. These values were chosen based on the findings of Belleguic et al. (2005), who analyzed gravity and topography data with the assumption of elastic support of surface loads in the lithosphere. In some studies, the density of the crust and the topography are treated separately (Beuthe et al., 2012), while here $\overline{\rho}_c$ is assigned to both, and the results should be interpreted accordingly.

We define the surface topography as a 2-dimensional map of elevation $h(\lambda,\phi)$, which are the measurements shown in Figure 1a. We computed the elevation profile of the crust-mantle boundary $r_c(\lambda,\phi)$ from surface topography using flexure modeling (Section 4.2), with the average crustal thickness set to $D_c = 60$ km. This value is consistent with that of M. A. Wieczorek and Zuber (2004), who computed geoid-to-topography ratios under the assumption of Airy isostasy, as well as with values later obtained from InSight seismic data (Drilleau et al., 2023) and the joint analysis of gravity, seismic and topography data (M. A. Wieczorek et al., 2022). The final element of the planetary model is the bottom boundary of the lithosphere, which was set to lie at a constant depth $D_l = 150$ km, which is the lithospheric thickness. This is consistent with the value used in the recent study by M. A. Wieczorek et al. (2022). This value does not represent a physical boundary, only the thickness of the layer in which lateral density variations were modeled, while the regions below this depth were assumed to have uniform densities. It was chosen to represent a relatively thin mantle layer that extends not far beyond the crust-mantle boundary. A thicker mantle with density fluctuations results in a higher overall contribution to the simulated gravity anomaly spectrum, as shown in Figure 3d. If mantle density variations are particularly high, they can dominate the signal and obscure the contribution from the crust, making the inference of crustal parameters more difficult. Assuming a thinner layer leads to a higher estimated SD of mantle density fluctuations from the analysis of real data. Therefore, the results must be interpreted in the context of the assumed D_l value.

Therefore, the planetary model outlined above defines the density distribution of the source $\rho(\boldsymbol{r})$ in Equation 3 as

$$\rho(\boldsymbol{r}) = \begin{cases} \rho_c(\lambda,\phi) & D_c + r_c(\lambda,\phi) < \omega < h(\lambda,\phi), \\ \rho_m(\lambda,\phi) & D_l < \omega < D_c + r_c(\lambda,\phi), \\ 0 & \omega < D_l. \end{cases} \tag{5}$$

It can be linked to the planet's gravitational field via gravity analysis using Equation 3.

4.1. The Density Distributions

For simulations of the lateral density distribution in the crust $\rho_c(\lambda,\phi)$ and the mantle $\rho_m(\lambda,\phi)$ we require a random process to generate physically viable density variations. The Matérn covariance function (Gneiting et al., 2010) is well-suited for this purpose when used to define multivariate normal distributions. The results can approximate natural patterns and the parameters of the function offer physically meaningful interpretations. The Matérn covariance function can be expressed on a sphere (Gneiting, 2013) with respect to the great circle distance, $\psi \in [0,\pi]$. We can express the Matérn covariance function as

$$M(\psi) = \frac{\sigma^2 2^{1-\kappa}}{\Gamma(\kappa)} (\alpha\psi)^{\kappa} \mathcal{K}_{\kappa}(\alpha\psi), \tag{6}$$

where $\mathcal{K}_{\kappa}$ is the modified Bessel function of the second kind, $\Gamma(\kappa)$ is the gamma function and σ is the SD. For $M(\psi)$ to be positive definite, the *scale parameter* α and *smoothness parameter* κ are restricted to the ranges $0 < \alpha$ and $0 < \kappa < \frac{1}{2}$. This limit imposed on the κ parameter is too restrictive for this analysis; therefore we invoke a

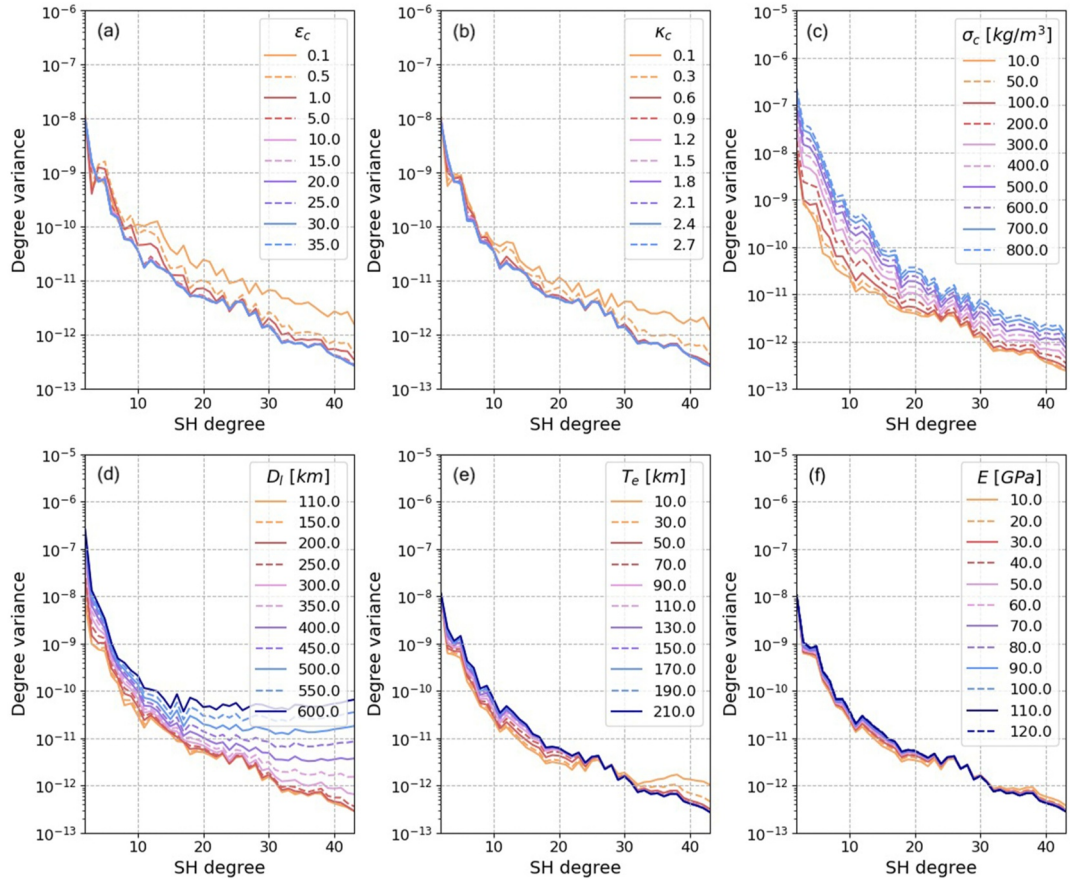

Figure 3. The effect of the Matérn and some of the flexure model parameters as well as the lithospheric thickness on the degree variance spectrum of the simulated gravitational field. (a)–(f) The parameters defining the density distribution in the crust (ϵ_c, κ_c, σ_c), the average thickness of the lithosphere (D_l) and the flexural response (T_e, E) were varied one by one while keeping all other parameters and the mantle density distribution constant. The Matérn parameters take the following values when not varied: $\epsilon = 5.0$, $\kappa = 0.6$, $\sigma = 100$ kg/m^3.

variation of the function, called the chordal Matérn covariance function, which redefines the covariance in terms of the chordal distance $2 \sin \frac{\psi}{2}$ (Guinness & Fuentes, 2015). In addition, we can introduce a reparametrization to break the existing coupling between the parameters α and κ by defining the de-*correlation distance* as $\epsilon = \frac{2\sqrt{\kappa}}{\alpha}$, which enables easier interpretation of the results. These changes lead to the expression

$$M_c(\psi) = \frac{\sigma^2 2^{1-\kappa}}{\Gamma(\kappa)} \left(\frac{4\sqrt{\kappa}}{\epsilon} \sin \frac{\psi}{2} \right)^{\kappa} \mathcal{K}_{\kappa} \left(\frac{4\sqrt{\kappa}}{\epsilon} \sin \frac{\psi}{2} \right), \tag{7}$$

which remains valid for all $\kappa > 0$.

The randomized density distribution maps required for the planetary model can be generated from multivariate normal distributions such as $\rho_c(\lambda, \phi) \sim \mathcal{N}(\overline{\rho}_c, M_c(\psi))$ and $\rho_m(\lambda, \phi) \sim \mathcal{N}(\overline{\rho}_m, M_c(\psi))$. The three parameters of interest that define the Matérn covariance function and govern the scale and structure of the density distributions are κ, ϵ and σ. Figure 4 illustrates the effect of the κ and ϵ parameters on the resulting density maps. These plots were all generated with the same random seed during the sampling of the normal distribution, to enable straightforward comparison. For instance, increasing the smoothness parameter κ results in a smoother distribution and lower overall amplitudes. Although the visual effect of the de-correlation distance ϵ is similar to κ, when examined more closely, it appears to play a role in forming connected and large-scale features. This is most apparent when observing the first row of Figure 4. In Figure 4a, where ϵ is relatively large ($\epsilon = 5.0$) and κ is low, connected regions appear in the data, with low values dominating the bottom-left and large values dominating the

21699100, 2026, 7, Downloaded from https://agupubs.onlinelibrary.wiley.com/doi/10.1029/2026JE009757 by Technical University Delft, Wiley Online Library on [30/07/2026]. See the Terms and Conditions (https://onlinelibrary.wiley.com/terms-and-conditions) on Wiley Online Library for rules of use; OA articles are governed by the applicable Creative Commons License

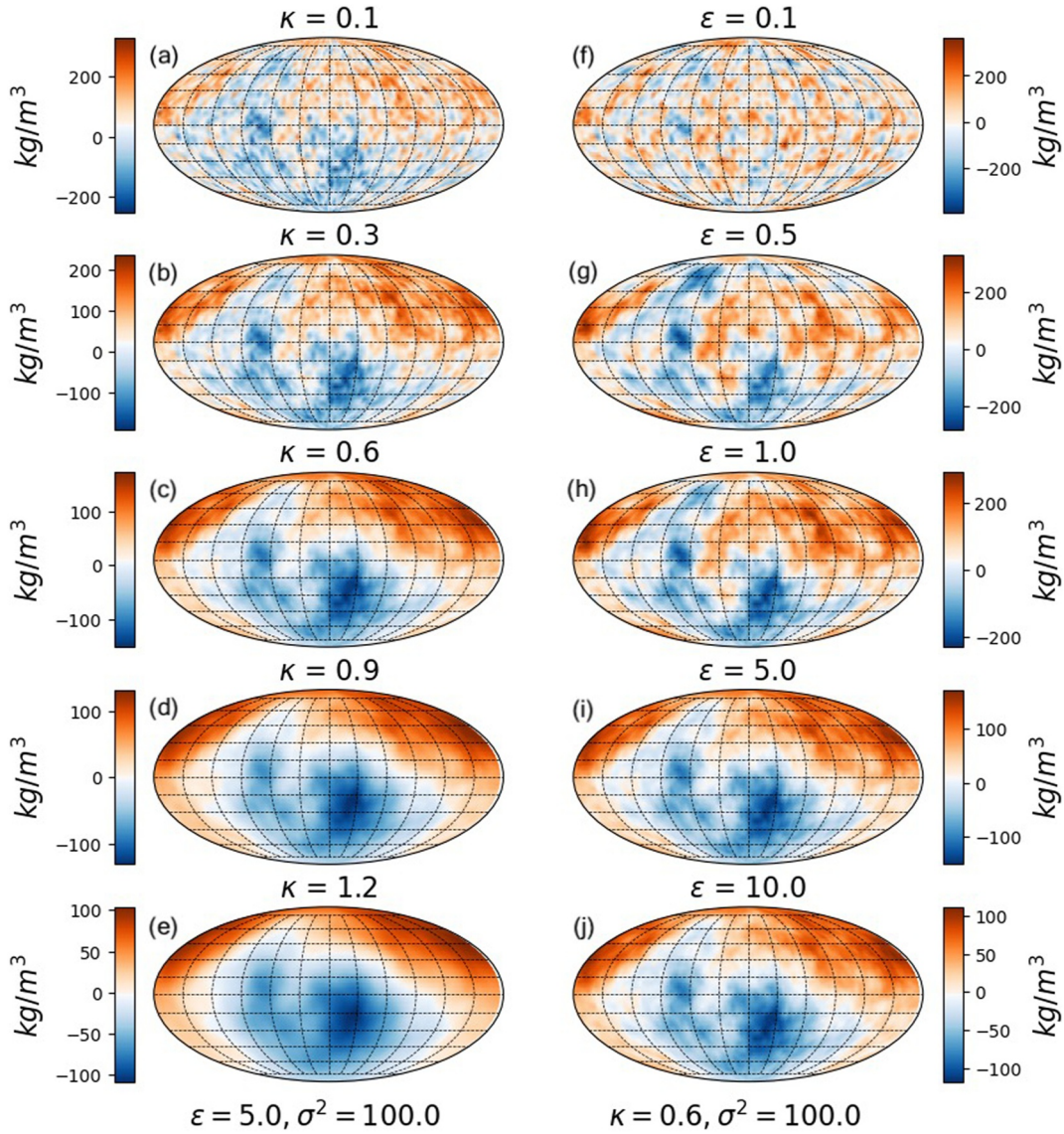

Figure 4. Map of density variations as a function of latitude and longitude on a sphere in the Mollweide projection. This plot visualizes the effect of the Matérn parameters κ in (a)–(e), and ϵ in (f)–(j) on the resulting lateral density maps generated from multivariate normal distributions. When varying one parameter, I kept the others constant, with $\kappa = 0.6$, $\epsilon = 5.0$ and $\sigma^2 = 100$ kg/m^3. The mean of the distribution is 0 kg/m^3. I kept the seed for the random sampling unaltered for comparability.

top-right of the map. On the other hand, a relatively high κ value ($\kappa = 0.6$) and a low ϵ value in Figure 4f results in largely uncorrelated noise and the absence of large-scale features. The third parameter, σ, directly controls the amplitude of the fluctuations in density.

It is important to note that these three parameters do not directly define the spatial distribution of densities, only some characteristics of the features of the distributions. Varying the random seed during sampling produces entirely different density map realizations, which share the same correlation matrix. Therefore, these are only similar in their smoothness and the scale of emerging connected features. This is demonstrated later in Figure 9, where several different random seeds were used to generate different density maps with agreeing Matérn parameters.

We chose the studied range of values for the Matérn parameters, listed in Table 1, based on the analysis of the simulated gravitational field's behavior with respect to these parameters. The effects of the crustal Matérn coefficients on the gravitational field degree variance spectrum are presented in Figure 3. Kaula's rule (Kaula, 1963),

21699100, 2026, 7, Downloaded from https://agupubs.onlinelibrary.wiley.com/doi/10.1029/2026JE009757 by Technical University Delft, Wiley Online Library on [30/07/2026]. See the Terms and Conditions (https://onlinelibrary.wiley.com/terms-and-conditions) on Wiley Online Library for rules of use; OA articles are governed by the applicable Creative Commons License

Table 1
The 3 Matérn Parameters That Define the Distribution of Lateral Density Variations in the Model of the Lithosphere of Mars and the Corresponding Lower and Upper Bounds of the Uniform Prior Probability Distributions Used in This Study

Parameter	Description	Lower bound	Upper bound
ϵ	De-correlation distance	0.1	20.0
κ	Smoothness parameter	0.1	1.5
σ	SD [kg/m^3]	100.0	500.0

based on empirical estimates, states that planetary gravitational spectra follow a power-law structure for planets with random internal density distributions (Ermakov et al., 2018). This relationship has also been confirmed for Mars from observations (Konopliv et al., 2016). However, the spectrum deviates from this power-law behavior due to isostatic compensation (Ermakov et al., 2018) and uncompensated large loads, such as Tharsis Rise (Phillips et al., 2001). The gravity degree variance spectra computed from the implemented planetary models broadly follow a power-law as well, but show some deviations due to the presence of larger-scale spatially correlated structures. The nature of these deviations vary with changes in the Matérn parameter values. In Figure 3b, we can observe that decreasing the value of the κ parameter has a flattening effect on the resulting gravity spectrum, meaning that at increasing SH degrees the downward gradient of the variance becomes less steep. This flattening effect starts at around 20 SH degrees. In Figure 3a the ϵ parameter has a similar effect, however, instead of a change in gradient, the spectrum undergoes an upward shift when the parameter is decreased. This effect becomes visually apparent at around 10 SH degrees. The upper bounds of the considered range for these two parameters were chosen as the values at which visual effects on the degree variance spectrum become indiscernible. Given the noise levels in the problem, later quantified in Section 6.2, any changes that are not visually discernible will fall well below the noise threshold. These bounds also correspond to the point where the relative change in the degree variance spectrum with respect to the preceding parameter value drops below 10%, as shown in Supporting Information S1. We set the lower bounds based on visual analysis of Figure 4. At the chosen parameter values, the small-scale features in the density distributions reach the $4° \times 4°$ resolution limit used in this work. As the σ parameter increases in Figure 3c, the degree variance spectrum shifts toward higher values, affecting the whole range of SH degrees. We chose the lower bound as an approximate where the effect of further changes in σ becomes insignificant and the higher bound based on a generous estimate of physically viable rock densities (Belleguic et al., 2005).

4.2. The Crust-Mantle Boundary

Isostasy models can be used to deduce $r_c(\lambda, \phi)$, the elevation profile of the crust-mantle boundary in the lithosphere, from the surface topography of the planet (Watts, 2023). In this work, we assumed laterally uniform densities for the crust and the mantle ($\overline{\rho}_c, \overline{\rho}_m$) during flexure modeling, and we only varied the thickness of the crust. In isostasy models, the lithosphere is usually represented as columns of material with varying densities and heights, split horizontally by the crust-mantle boundary. The simplest models, such as the Airy model (Airy, 1855), assume local compensation, where the columns of material can move independently without friction. Regional compensation or flexure models assume that the weight of the load is compensated over longer distances. The lithosphere can be represented as a thin layer floating on viscous material, which deforms in response to the applied load. Two notable flexure models are the infinite plate model (Watts, 2023) and the thin shell model (Kraus, 1967). Given its relatively small size and large topographic features, the curvature of Mars is not negligible. Therefore, we applied the thin shell model in this study, which accounts for the effects of the curvature.

The flexure response function is defined in the textbook by Watts (2023) as the ratio of the deflection of the lithosphere and the applied load, with values in the range of [0, 1] quantifying the level of compensation. The flexure response of the thin shell model was derived by Root et al. (2026) in the following form;

$$\Phi(n)_f = \left[1 + \frac{D}{(\overline{\rho}_m - \overline{\rho}_c)g}\left(\frac{1}{R_\mathcal{S}^4}\frac{[n(n+1)-2]^2}{1-\frac{1-\nu}{n(n+1)}} + 12\frac{1-\nu^2}{T_e^2 R_\mathcal{S}^2}\frac{1-\frac{2}{n(n+1)}}{1-\frac{1-\nu}{n(n+1)}}\right)\right]^{-1}, \quad (8)$$

where g is the gravitational acceleration and ν is the Poisson's ratio. The flexural rigidity D is defined as

$$D = \frac{ETe^3}{12(1-\nu^2)}, \quad (9)$$

21699100, 2026, 7, Downloaded from https://agupubs.onlinelibrary.wiley.com/doi/10.1029/2026JE009757 by Technical University Delft, Wiley Online Library on [30/07/2026]. See the Terms and Conditions (https://onlinelibrary.wiley.com/terms-and-conditions) on Wiley Online Library for rules of use; OA articles are governed by the applicable Creative Commons License

21699100, 2026, 7, Downloaded from https://agupubs.onlinelibrary.wiley.com/doi/10.1029/2026JE009757 by Technical University Delft, Wiley Online Library on [30/07/2026]. See the Terms and Conditions (https://onlinelibrary.wiley.com/terms-and-conditions) on Wiley Online Library for rules of use; OA articles are governed by the applicable Creative Commons License

with E representing Young's modulus. The rigidity of the lithosphere is also controlled by the effective elastic thickness T_e. This determines the level of deformation, with higher values describing a more rigid lithosphere, while for low values of T_e, the flexure models converge to local compensation models. As discussed by Mussini (2019); Root et al. (2026), we can view the flexure response function as a filter acting on the crustal thickness profile in the SH domain obtained from Airy isostasy A_{nm} (Airy, 1855), such that

$$F_{nm} = A_{nm}\Phi(n)_f, \tag{10}$$

where A_{nm} can be obtained from the elevation profile defined by Airy isostasy,

$$r_{c,A}(\lambda,\phi) = \frac{\overline{\rho}_c h(\lambda,\phi)}{\overline{\rho}_m - \overline{\rho}_c}, \tag{11}$$

using GSHA. We can obtain the spatial variation of the crust–mantle boundary $r_{c,f}(\lambda,\phi)$ from the SH coefficients F_{nm} using GSHS.

The elastic thickness of the lithosphere is ill-constrained and the predicted values are highly variable. In this study, we implemented a single global value of $T_e = 80$ km, which is consistent with the range of possible values identified by a number of studies (Grott & Breuer, 2008; Taylor et al., 2020; Turcotte et al., 2002). We also applied the commonly used value of Young's modulus ($E = 100$ GPa) here, but some studies suggest that this value might be significantly lower (Taylor et al., 2020). Additionally, we set Poisson's ratio to be $\nu = 0.25$, which is the generally accepted value in the literature (Belleguic et al., 2005; Beuthe et al., 2012; McGovern et al., 2004). Due to incomplete knowledge, the adopted values for the E and T_e parameters might correspond to the true values for the Martian lithosphere. However, it is shown in Figures 3e and 3f that these parameters do not have a significant influence on the gravity degree variance spectrum. The impact of the T_e parameter (Figure 3e) becomes discernible when $T_e < 30$ km. While this is still within the range of some local estimates from for example, thermal evolution models (Grott & Breuer, 2008), a value below 50 km for the global average is not likely.

We applied the thin shell flexure model to compute the crust-mantle boundary from the surface topography of Mars, using the `topo2crust` function in the `GSH` Matlab package (Root, 2021). The map of the elevation profile of the Martian crust–mantle boundary, shown in Figure 1b, is largely consistent with crustal thickness maps from previous gravity and topography studies (Bozdag et al., 2017; G. A. Neumann et al., 2004; M. A. Wieczorek & Zuber, 2004), differing only due to deviations in the assumed mean crustal thickness D_c and density $\overline{\rho}_c$. The thick crust in the model (>100 km) beneath the Tharsis Rise region arises from the presence of large surface loads (Phillips et al., 2001), while the thin crust beneath Hellas Planitia and in the northern hemisphere is consistent with the low topography in these areas.

5. Bayesian Gravity Analysis Method

The aim of this work is to obtain a probability distribution of Matérn coefficients describing the density distributions in the lithosphere of Mars from gravity measurements. This question can be formulated as a Bayesian parameter inference problem, where the posterior probability distribution function (PDF) of the Matérn parameters can be obtained via Bayes' Theorem (Bayes, 1763), which describes the posterior PDF, $p(\boldsymbol{\theta}|\boldsymbol{d},A)$ as

$$p(\boldsymbol{\theta}|\boldsymbol{d},A) = \frac{p(\boldsymbol{\theta}|A)p(\boldsymbol{d}|\boldsymbol{\theta},A)}{p(\boldsymbol{d}|A)}, \tag{12}$$

where $\pi(\boldsymbol{\theta}) \equiv p(\boldsymbol{\theta}|A)$ is the prior and $L(\boldsymbol{\theta}) \equiv p(\boldsymbol{d}|\boldsymbol{\theta},A)$ is the likelihood. The prior distribution describes our knowledge of the problem, before obtaining any data, while the likelihood is the measure of how well a particular set of parameters explains the observed data. The denominator is a normalizing constant, called the Bayesian evidence. In this problem, $\boldsymbol{\theta}$ are the Matérn parameters and $\boldsymbol{d}$ stands for the measurements or simulations of the gravitational field in a degree variance spectrum format. The forward model A links the parameters $\boldsymbol{\theta}$ to the degree variance spectra of the gravitational field, which was described in Sections 4 and 3.

If the forward model A is linear, the evidence and the posterior can be expressed analytically. However, in this case A is non-linear, hence it is not possible to obtain an analytical expression and we need to approximate the

21699100, 2026, 7, Downloaded from https://agupubs.onlinelibrary.wiley.com/doi/10.1029/2026JE009757 by Technical University Delft, Wiley Online Library on [30/07/2026]. See the Terms and Conditions (https://onlinelibrary.wiley.com/terms-and-conditions) on Wiley Online Library for rules of use; OA articles are governed by the applicable Creative Commons License

evidence or avoid computing it altogether. Most commonly sampling methods are applied to approximate the posterior, such as MCMC, however, these require either an analytical expression or a numerical approximation of the likelihood function. In this problem the likelihood is untractable, therefore, likelihood-free inference is an attractive choice for this problem. The Normalizing Flow (NF) approach to Bayesian inference offers a promising solution, as it approximates the posterior using a data-driven approach.

5.1. Normalizing Flows

NFs (Rezende & Mohamed, 2016) are a type of generative neural network that are ideally suited for the modeling and sampling of complex data distributions. The basis of the method, as described by Papamakarios et al. (2021), is to express the data vector $\boldsymbol{\theta}$ as a transformation T of another vector $\boldsymbol{u}$, which is sampled from an arbitrary base distribution $p_u(\boldsymbol{u})$. Then, we can define the PDF of $\boldsymbol{\theta}$ via the change of variables formula

$$\begin{aligned} p_\theta(\boldsymbol{\theta}) &= p_u(\boldsymbol{u})|\det J_T(\boldsymbol{u})|^{-1} \\ &= p_u\left(T^{-1}(\boldsymbol{\theta})\right)|\det J_{T^{-1}}(\boldsymbol{\theta})|, \end{aligned} \tag{13}$$

where J_T is the Jacobian matrix containing the partial derivatives of T with respect to $\boldsymbol{u}$.

To be able to model rich and complex PDFs, T can be a composite transformation made up of a number of invertible and differentiable functions. These stacked transformations are often implemented as a neural network with trainable parameters $\boldsymbol{\phi}$. The network parameters are iteratively tuned during training with the aim to minimize the loss function $\mathcal{L}$, which is defined as the Kullback-Leibler (KL) divergence between the network output $q_\theta(\boldsymbol{\theta};\boldsymbol{\phi})$ and the target distribution $p_\theta(\boldsymbol{\theta})$.

During each training iteration, the loss is computed from N target distribution samples, where N is defined by the *batch size*. Then, the gradient of the loss with respect to the trainable parameters $\boldsymbol{\phi}$ is computed and $\boldsymbol{\phi}$ are optimized using stochastic gradient-based methods (Kingma & Ba, 2017). When the network is fully trained, the output of the last transformation layer in the normalizing direction, usually referred to as the *latent space* $q_u(\boldsymbol{u})$, is equal to the base distribution, $p_u(\boldsymbol{u}) = q_u(\boldsymbol{u})$. Since we can choose $p_u(\boldsymbol{u})$ freely, it is beneficial to opt for a distribution which can be cheaply sampled from, hence we often set it to be a multi-dimensional unit Gaussian. Samples from the base distribution can then be passed through the transformations in the generative direction, enabling efficient sampling from the data distribution.

The algorithm described above is a generative model which can be used to interpolate a discrete data set and generate samples from the resulting continuous distribution. However, to apply this method to parameter inference, we need to introduce a *conditional* input alongside the training data. Assume that the aim is to infer the posterior PDF of some parameters $\boldsymbol{\theta}$ conditioned on some observation $\boldsymbol{d}$. Then, we can train the NF to approximate the conditional posterior PDF $p(\boldsymbol{\theta}|\boldsymbol{d},A)$, such that

$$p_\theta(\boldsymbol{\theta}|\boldsymbol{d},A) \approx q_\theta(\boldsymbol{\theta};\boldsymbol{\phi}|\boldsymbol{d}) = p(\boldsymbol{u})\det|J_T(\boldsymbol{u};\boldsymbol{\phi}|\boldsymbol{d})|^{-1}. \tag{14}$$

To apply this method to gravity analysis, we need to generate a data set of source parameters $\boldsymbol{\theta}$ from the chosen prior distribution. Then, we can simulate the corresponding gravity measurements $\boldsymbol{d}$ via the gravity forward model A, forming the conditional part of the input. Once the network is trained on this data set, we can generate samples from the posterior distribution of source parameters conditioned on a specific gravity spectrum of interest. If the method performs well, these samples are consistent with the input gravity spectrum, within the uncertainties arising from non-uniqueness and other modeled noise effects.

A more in-depth review of the development history of different NF architectures, and further considerations when constructing and training such networks is available in the review article by Kobyzev et al. (2021). A widely applied and highly expressive NF architecture, real-valued non-volume preserving (RealNVP) (Dinh et al., 2017), was used in this work.

5.2. Network Architecture and Training Methodology

The RealNVP architecture is implemented here using `glasflow` (Williams et al., 2023), a Python package built upon `nflows` (Durkan et al., 2020) and `pytorch` (Paszke et al., 2019). The full software is available on Github

Table 2
The Parameters That Define the RealNVP Neural Network Architecture Implemented in This Chapter

Parameter	Value
Number of transforms	23
Number of blocks per transform	8
Number of neurons	20
Batch size	10^4
Initial learning rate	10^{-3}

Note. Only the parameters that differ from the default values in `glasflow` (Williams et al., 2023) are listed here.

(Rakoczi, 2026). The parameters defining the network structure are listed in Table 2. We trained the network using the built-in `pytorch Adam` optimizer (Kingma & Ba, 2017) and the `ReduceLRonPlateau` learning rate scheduler. The scheduler was set up such that the learning rate was multiplied by a factor of 0.05 whenever the validation loss reached a plateau and did not decrease for at least 100 epochs, starting from the initial learning rate shown in Table 2. We considered the training complete when the minimum learning rate of 10^{-6} was reached, which was achieved after 10^4 epochs corresponding to ∼2 days of training using an NVIDIA GeForce RTX 4090 graphics card.

The data set is 6-dimensional and consists of different realizations of Matérn parameters for the two layers, $\boldsymbol{\theta} = \{\epsilon_c, \kappa_c, \sigma_c\, \epsilon_m, \kappa_m, \sigma_m\}$, generated from the prior distributions in Table 1. The conditional input is the degree variance curve of the simulated gravitational fields and has the dimensionality of 39, where the degrees $n \leq 7$ were removed for normalization, as explained in Section 3. Each degree variance curve includes the real measurement noise. Therefore, the conditional input $\boldsymbol{d}$ corresponding to each set of parameters in the data $\boldsymbol{\theta}$ is the noisy degree variance spectrum of the simulated planet's gravitational field. We trained the network using 10^7 training samples and tested using 10^6 samples as validation data. We normalized the input data, consisting of the Matérn parameters $\boldsymbol{\theta} = \{\epsilon_c, \kappa_c, \sigma_c\}$ sampled from the corresponding prior distributions, to the [0,1] range using the `scikit-learn MinMaxScaler` method, separately for the three parameters. In addition, we scaled the conditional inputs $\boldsymbol{d}$, consisting of the gravity degree variance spectra corresponding to each set of Matérn parameters, using `QuantileTransformer`. The `QuantileTransformer` method computes the cumulative distribution function (CDF) of each feature separately, where each feature corresponds to an SH degree in the spectrum, and maps the data to a uniform distribution over the interval [0, 1]. For this, we set the number of quantiles to 10^4. The `QuantileTransformer` helps make data on different scales more comparable, which is important for this data set, as the degree variance spectra contain values at several different orders of magnitude.

Once the network is trained, we can generate samples conditioned on any gravity spectrum of interest that is consistent with the training data set. Samples from the posterior can be generated rapidly, with 2,000 samples within ∼10 ms.

6. Validation of the Posterior Distribution

It is important to validate the trained neural network to determine its performance in parameter inference. First, we need to test whether the posterior distributions produced by the NF inference are statistically consistent, meaning that the posterior distribution is not over- or under-constrained, nor skewed. Then, we need to understand what level of accuracy we can expect from the output of the inference, given the level of noise present in the problem. Given this understanding of the noise level, when we perform the inference with the gravity spectrum of Mars, we can evaluate the agreement between the posterior samples and the input. Testing with synthetic data is included as Supporting Information S1, which is not directly relevant for the interpretation of the results, but can serve as further validation of the technique.

6.1. Statistical Consistency of the Posterior

It is important to verify that the resulting posterior PDFs are statistically consistent and unbiased. A suitable visualization is a probability–probability (p–p) plot, a standard method used to validate Bayesian algorithms (Cook et al., 2006; Talts et al., 2020). This test, based on a frequentist statistical framework, evaluates the frequency K with which the true parameter value falls within the K% credible interval of the posterior PDF for an ensemble of inputs. To construct the p-p plot shown in Figure 5, the following process was applied; first, 100 sets of source parameters were generated from the prior and were forward-modeled to compute simulated gravity surveys. These constitute a set of gravimetry surveys consistent with the prior distributions used in the inference. Then, each survey was used to generate 2,000 samples from the posterior distribution of source parameters. The value of the marginalized CDF at the true parameter location in each dimension was then calculated separately for each test case. The distribution of the CDFs at the true parameter values across all test cases approaches a uniform distribution when the method is consistent. Then, computing the CDF of these (ideally) uniform distributions

21699100, 2026, 7, Downloaded from https://agupubs.onlinelibrary.wiley.com/doi/10.1029/2026JE009757 by Technical University Delft, Wiley Online Library on [30/07/2026]. See the Terms and Conditions (https://onlinelibrary.wiley.com/terms-and-conditions) on Wiley Online Library for rules of use; OA articles are governed by the applicable Creative Commons License

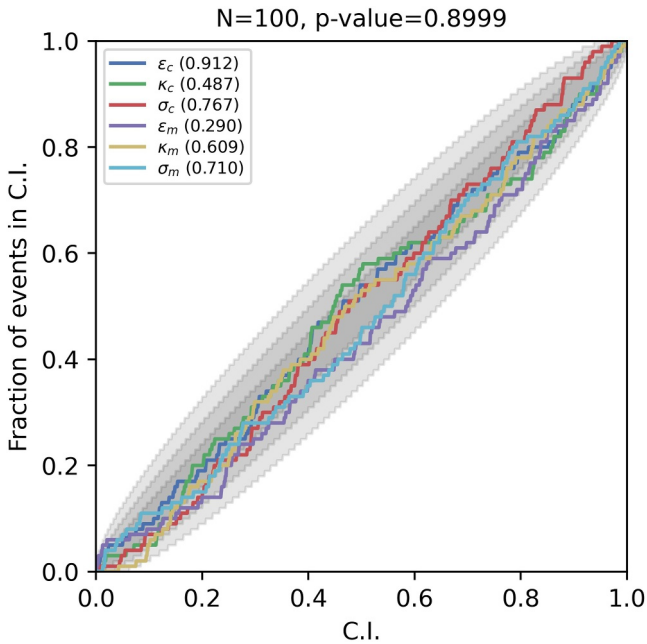

Figure 5. The p-p plot obtained from the testing of the two-layer NF parameter inference tool. The statistical consistency is tested for each of the 1-dimensional marginal probability distributions of the parameters separately, as indicated by the curves in different colors. The *p*-values are listed in the legend for each dimension and the combined value is displayed above each graph. The gray regions correspond to the 68%, 95%, and 99.7% confidence intervals.

produces a series of lines that follow the diagonal. However, since a relatively small number of test cases was used to construct this plot, slight deviations from the diagonal are expected. We consider the inference method statistically consistent as long as the curves remain within the 68%, 95%, and 99.7% confidence intervals, indicated by the gray regions on the plot.

A more rigorous measure, the *p*-value, was also computed using the Kolmogorov-Smirnov (KS) statistic, which measures the maximum vertical distance between the diagonal and the curves corresponding to the various parameter dimensions. The p-value is then obtained from the KS distribution, representing the probability that the KS statistic is equal to or greater than the KS value obtained under the null hypothesis that the underlying CDF is diagonal. Very small *p*-values indicate that the null hypothesis is unlikely. The combined value displayed at the top is obtained using Fisher's method, which computes the *p*-value with the null hypothesis that each parameter independently satisfies its own null hypothesis. Ideally, the *p*-values for each dimension, as well as the combined value, are all expected to behave as random samples from a uniform distribution between 0 and 1. Figure 5 presents evidence that the NF inference method produces statistically consistent posterior probability distributions.

6.2. Sources of Noise

There are two noise sources that affect the degree variance spectra; the noise originating from the randomization of the density distributions, and the instrumental noise from the measurements of the gravity field. All noise aspects need to be taken into consideration when evaluating the performance of the network and the accuracy of the inference, as we cannot expect it to outperform these limitations. Firstly, a single set of Matérn parameters and the corresponding covariance matrix were used to generate random samples from a multivariate normal distribution to obtain lateral density distributions in the crust. Due to this randomization, the mapping between the Matérn parameters and the gravitation field is not deterministic, and the same set of parameters can result in a range of degree variance spectra. Intuitively, when the SD of the density fluctuations σ_c increases, the noise introduced by the randomization of these fluctuations also shifts to a higher level. We demonstrate this effect in Figure 6, where we show the element-wise SD of 100 degree variance spectra arising due to density fluctuations. There is a similar effect due to changes in σ_m, but less pronounced. Secondly, there is measurement noise originating from hardware and the solar plasma noise (Konopliv et al., 2016). The

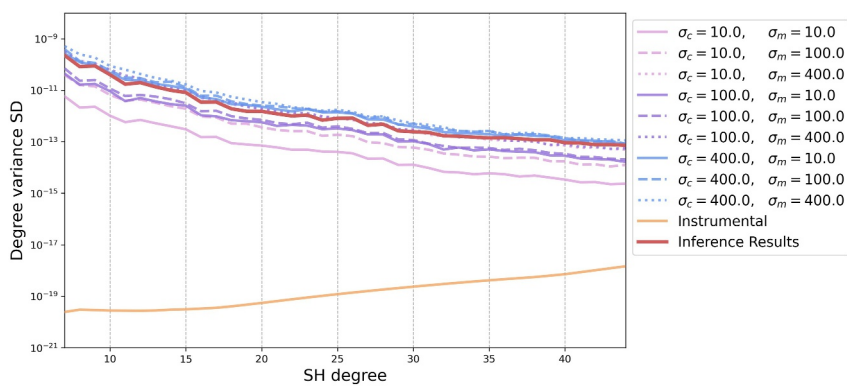

Figure 6. Degree variance spectra of the SD for different noise sources. Instrumental noise is shown in yellow and the noise arising from different values of σ in the crust and mantle is shown in pink, purple, and blue based on σ_c, with different linestyles indicating the value of σ_m. All the σ values are given in the units kg/m^3. These are compared to the SD of gravity spectra simulated from samples from the inference results, shown in red.

21699100, 2026, 7, Downloaded from https://agupubs.onlinelibrary.wiley.com/doi/10.1029/2026JE009757 by Technical University Delft, Wiley Online Library on [30/07/2026]. See the Terms and Conditions (https://onlinelibrary.wiley.com/terms-and-conditions) on Wiley Online Library for rules of use; OA articles are governed by the applicable Creative Commons License

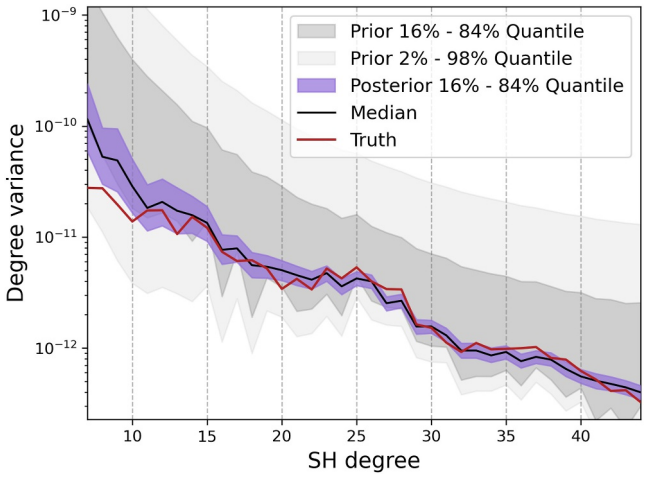

Figure 7. The observed gravity degree spectrum of Mars (red), which is the input to the inference, is compared to statistics obtained from 10^3 samples generated from the two-layer NF inference method. The median (black) and the 16%–18% quantile regions (purple) were computed element-wise for each degree. The output is also compared to the high-probability regions of the conditional inputs in the training set, marked in gray.

instrumental noise spectrum, calculated using Equation 4, is also shown in Figure 6, and it is apparent that the effect is orders of magnitude smaller compared to the noise from the randomized densities.

6.3. Agreement Between the Posterior Samples and the Input

We can now evaluate whether the predicted Matérn coefficient values are consistent with the conditional input within the noise limitations of the problem. We can take samples from the posterior probability distribution and feed them through the forward modeling method to generate simulated observations. For these tests, we drew 10^3 samples from the 3-dimensional posterior distribution modeled by the NF conditioned on the red degree variance spectrum in Figure 7. The NF inversion does not always respect the bounds of the prior space, and it may return samples that lie outside the prior. These samples do not correspond to physically viable planetary models; hence, these were discarded. In this case, we found 12.4% of the samples drawn from the NF to lie outside the bounds of the prior space, which is low enough not to significantly affect the results. Once we obtained the degree variance spectra for each sample, we computed the element-wise median and 16%–84% quantile ranges for each degree of the spectra. Figure 7 shows the results, where the true degree variance values are matched by the samples for SH degrees above ∼10, with an accuracy consistent with the expected noise levels (Figure 6). However, there is a power excess in the results of the inference at low SH degrees. As shown in Supporting Information S1, this disagreement is not present when the method is tested using simulated data consistent with the training set, suggesting a mismatch between the simulations and the real structure of Mars. This inconsistency most likely originates from incomplete planetary models. As discussed in Section 3, the SH degrees $n < 7$ were discarded during the analysis due to the existence of a large mantle plume on Mars, which affects the degree variance spectrum at low SH degrees, but was not included in the planetary models. It is possible that this feature has an effect on the gravitational field at even higher degrees, resulting in this mismatch at $n < 10$. For the rest of this analysis, we assume that the simulated planetary models are broadly correct but overly simplistic, and that any deviations from the real gravity degree variance curve arise from additional features not included in the synthetic model. With this assumption, we can use the posterior probability distributions of the Matérn parameters to study the lithospheric structure of Mars.

7. Results

The corner plot in Figure 8 presents the posterior probability distribution of the Matérn parameters in the crust and the mantle of Mars. It is important to note that we should not expect the true parameter values to coincide with the highest-probability point in the posterior, only that it should fall within the high-probability regions for the majority of cases. This is the expected behavior of a statistically consistent inference, as demonstrated by the p-p plot in Figure 5. Similarly, the samples within the high-probability regions of the posterior are not expected to best reproduce the input spectrum as all samples should agree with the input within the noise limitations of the problem.

In the posterior distribution we can observe that the 1-dimensional marginalized distributions of the κ and σ parameters are relatively narrow, while the distribution of ϵ is broader, which suggests that the measured gravity spectra are least sensitive to the parameter corresponding to the decorrelation distance. Both κ values are relatively well-constrained, with $\kappa_c = 0.24^{+0.08}_{-0.06}$ and $\kappa_m = 1.30^{+0.15}_{-0.32}$. In 97.75% of the samples drawn from the NF, $\kappa_c < \kappa_m$, indicating that the mantle density distribution is likely to be smoother with more diffuse patterns and fewer abrupt changes. While the de-correlation distances ϵ_c and ϵ_m are not tightly constrained, they are more likely to take high values with $\epsilon_c > 5.83$ and $\epsilon_m > 10.81$, where the bounds correspond to the 16% quantile. This suggests that there are large connected structures present in both layers. In the ϵ_c and ϵ_m dimensions, the mode of the distribution falls very close to the upper boundary of the prior, while in the κ_m dimension the mode falls right at or even beyond the upper bound. This suggests that the data favour larger parameter values, potentially exceeding the prior boundaries indicated by the axis limits. However, values above this threshold cannot be distinguished

21699100, 2026, 7, Downloaded from https://agupubs.onlinelibrary.wiley.com/doi/10.1029/2026JE009757 by Technical University Delft, Wiley Online Library on [30/07/2026]. See the Terms and Conditions (https://onlinelibrary.wiley.com/terms-and-conditions) on Wiley Online Library for rules of use; OA articles are governed by the applicable Creative Commons License

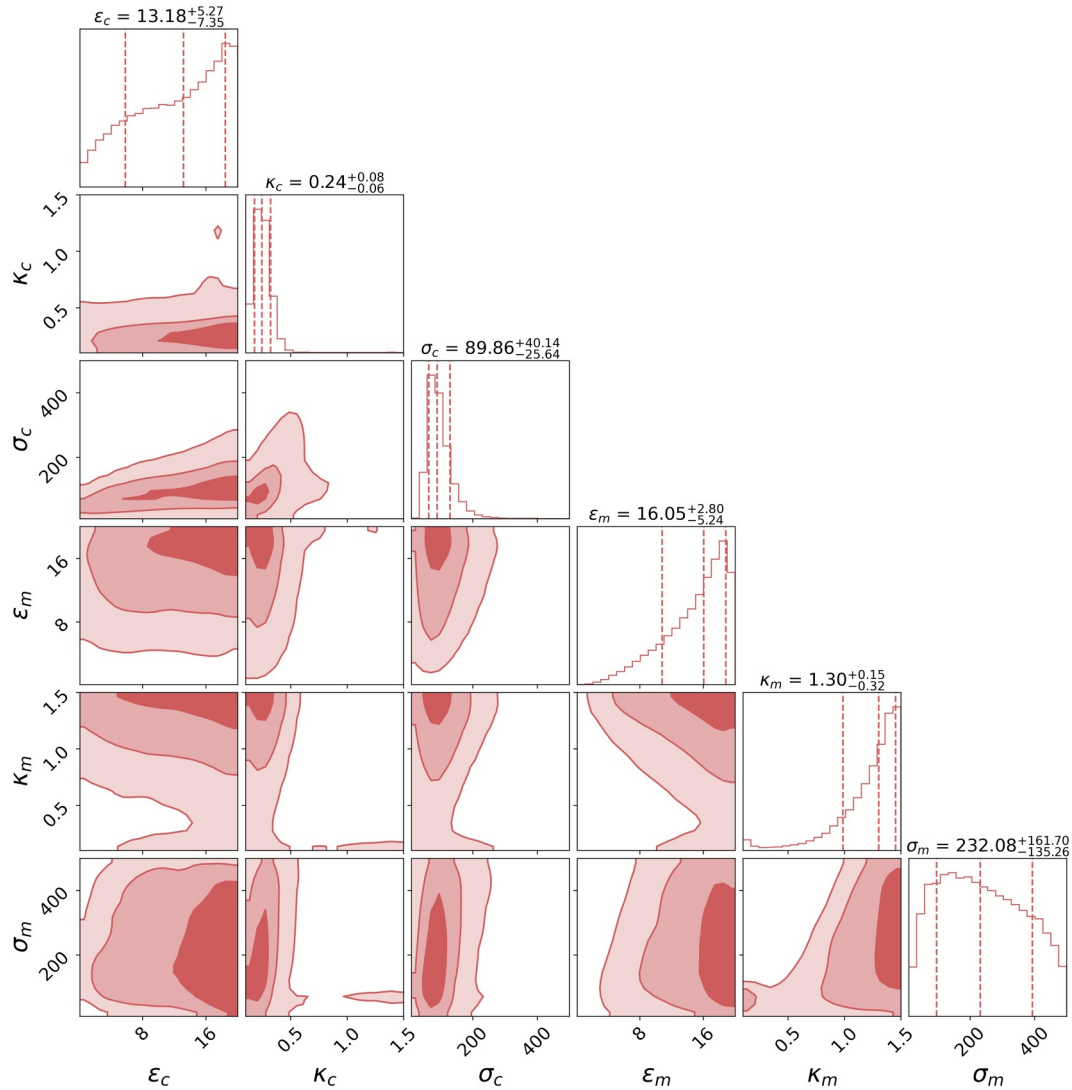

Figure 8. Corner plot showing the posterior probability distribution of the Matérn parameters of the density distributions in the crust and the mantle from the inference using the gravity degree variance curve of Mars, shown in Figure 7, as the input. The 1-dimensional marginalized probability distributions of each of the parameters are displayed on the diagonal. The median values of the 1-dimensional distributions from the NF inference are displayed above each plot. The dashed lines and the numerical error bounds correspond to the 16% and 84% quantiles of the distribution. Below the diagonal, 2-dimensional joint distributions of the parameter pairs are shown. The probability contours correspond to the 0.393 (1σ), 0.865 (2σ) and 0.989 (4.5σ) confidence regions. The axis limits are set to the prior boundaries for each parameter.

because the sensitivity of the observations is limited by noise, as discussed in Section 4.1. Consequently, we should interpret these results as lower bounds rather than well-constrained estimates of these parameters. Additional data sources would be needed to constrain them further. The SD in the mantle σ_m is also not well-constrained, however, σ_c is predicted to lie in the 90^{+40}_{-26} kg/m^3 range, providing a constraint for the density values in the crust. In addition to the numerical constraints on the parameters derived from the 1-dimensional distributions, the joint distributions below the diagonal provide additional insight into correlations between parameter pairs. For instance, we can observe a slight positive correlation between the κ_c and σ_c parameters. This relationship indicates that when the density distribution is smoother, larger amplitude fluctuations are needed to generate the same gravity signature.

To visualize the implications of the results, we generated different realizations of the density maps from the mode of the posterior PDF, approximated by the highest likelihood sample from 10^7 random draws. We generated each

21699100, 2026, 7, Downloaded from https://agupubs.onlinelibrary.wiley.com/doi/10.1029/2026JE009757 by Technical University Delft, Wiley Online Library on [30/07/2026]. See the Terms and Conditions (https://onlinelibrary.wiley.com/terms-and-conditions) on Wiley Online Library for rules of use; OA articles are governed by the applicable Creative Commons License

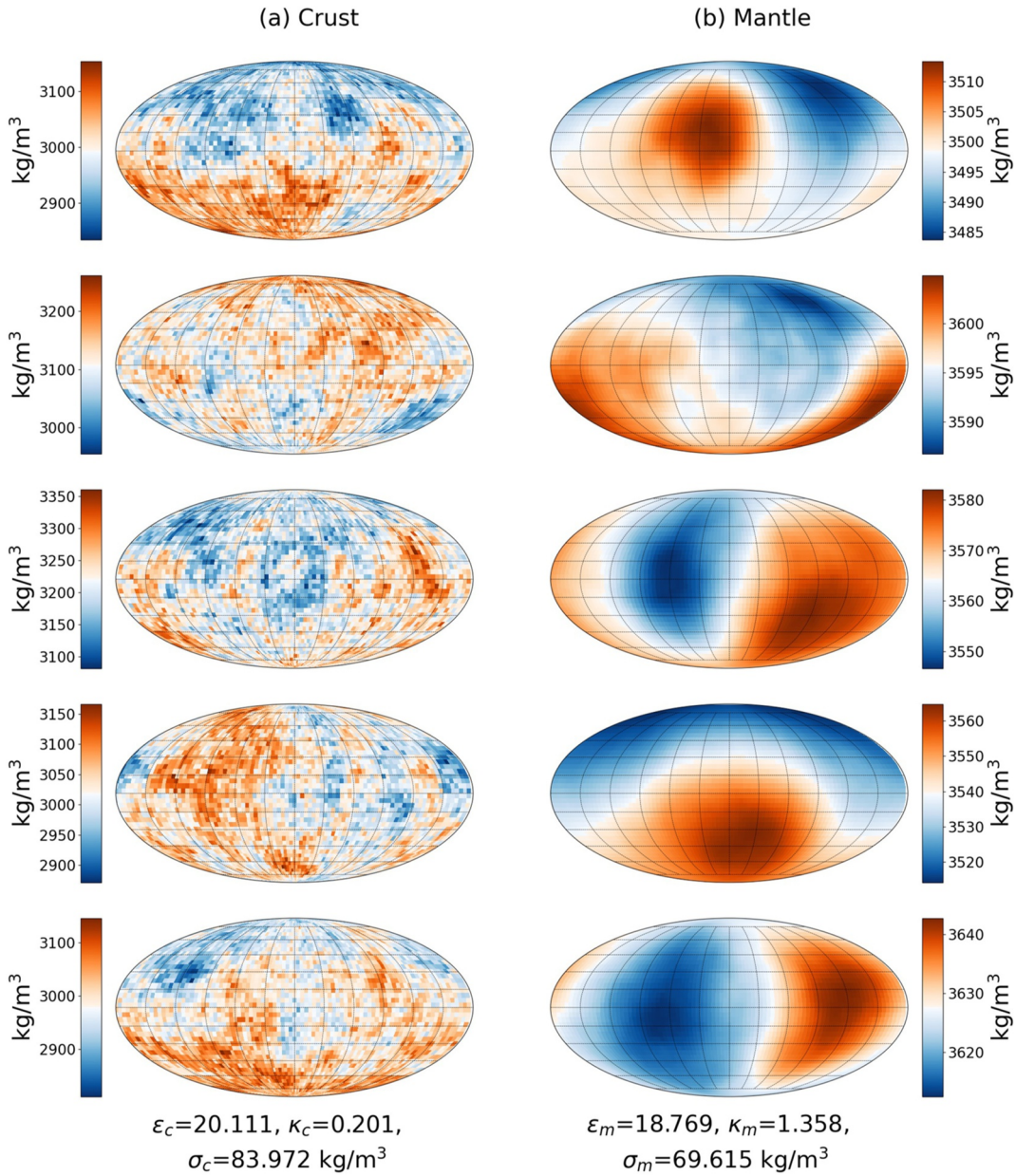

Figure 9. Different realizations of the lateral density maps in (a) the crust ($\rho_c(\lambda,\phi)$) and (b) the mantle ($\rho_m(\lambda,\phi)$) from the mode of the posterior probability distributions of the Matérn parameters from the inference using the gravity degree variance spectrum of Mars. The seed number used to sample the multivariate normal distribution was varied between each row, while the covariance matrix, defined by the Matérn parameters listed below, was kept unchanged.

plot in Figure 9 with a different seed for the multivariate sampling, representing possible density configurations corresponding to the results of this analysis. The maps in Figure 9b further illustrate the earlier conclusion that the mantle features smoother structures compared to the crust. They indicate large-scale density variations in the mantle with smooth transitions and the presence of extensive, connected features spanning thousands of kilometers. In the crust (Figure 9a), correlated density features can also span thousands of kilometers, but finer, more localized structures appear on scales of hundreds of kilometers.

As no prior studies have computed the Matérn parameters for Martian lithospheric densities, a direct comparison is not possible. However, we can obtain the range of variation in the global crustal and mantle densities from the generated density maps and compare them with the values from different studies. For this purpose, we drew 100

21699100, 2026, 7, Downloaded from https://agupubs.onlinelibrary.wiley.com/doi/10.1029/2026JE009757 by Technical University Delft, Wiley Online Library on [30/07/2026]. See the Terms and Conditions (https://onlinelibrary.wiley.com/terms-and-conditions) on Wiley Online Library for rules of use; OA articles are governed by the applicable Creative Commons License

21699100, 2026, 7, Downloaded from https://agupubs.onlinelibrary.wiley.com/doi/10.1029/2026JE009757 by Technical University Delft, Wiley Online Library on [30/07/2026]. See the Terms and Conditions (https://onlinelibrary.wiley.com/terms-and-conditions) on Wiley Online Library for rules of use; OA articles are governed by the applicable Creative Commons License

random samples from the posterior PDF of the Matérn parameters shown in Figure 8 and examined the resulting variations in the corresponding density maps. We found the crustal and mantle densities to fall in the 3042^{+93}_{-98} kg/m^3 and the 3544^{+304}_{-221} kg/m^3 range, correspondingly. Recall that a relatively thin lithosphere was used in the model with D_l =150 km. This would not affect the parameters defining the spatial correlations in the mantle, κ_m and ϵ_m, but it does increase the SD of the density fluctuations, causing the maxima and minima in the mantle to be larger than for a thicker lithosphere. We found the resulting density range to be very broad and to provide limited information. A different approach is to generate 100 maps from the mode of the distribution only, leading to crustal densities in the range of 3036^{+87}_{-89} kg/m^3 and mantle densities of 3525^{+111}_{-78} kg/m^3. However, since the σ_m parameter is poorly constrained and directly influences the range of mantle densities, the value inferred from the mode of its distribution cannot be regarded with high confidence. It is worth noting that the obtained crustal density ranges largely overlap with earlier studies (McGovern et al., 2004; Pauer & Breuer, 2008; Turcotte et al., 2002). In addition, the inferred crustal and mantle density ranges are in close agreement with those reported by Drilleau et al. (2024), who jointly inverted seismological and gravity data.

The resulting posterior probability distributions provide some constraints on the values of the individual parameters governing the planet's density distribution. In addition, the inference significantly narrowed the probability space of the potential parameter values. One way to quantify the reduction of the parameter space is to compare the volumes of the prior and posterior distributions of the Matérn parameters. We use the volume reduction measure given by the percentage of the prior volume contained within the 68% (1σ) and 95% (2σ) confidence intervals of the posterior probability distribution obtained from the inference. To compute the volume reduction for the 68% interval, we drew samples from the prior distribution and counted the number of samples contained within the 68% confidence interval of the posterior PDF. Then, we define the volume reduction measure as the percentage of the prior samples contained within this high-probability region of the posterior. We repeated the same method for the 95% confidence interval. A lower percentage indicates a higher reduction in volume during inference. To sufficiently explore the probability space, we used 10^7 samples to compute this metric. The volume reduction for the posterior distribution in Figure 8 is 0.09% and 0.33% corresponding to the two confidence regions, where a 0.09% volume reduction means that the volume within the 68% posterior confidence interval is 0.09% of the prior volume.

8. Discussion

In this study, we constructed the planetary models using a combination of simulated density distributions, flexure modeling, and topography data from Mars. Then, we computed the gravitational fields of these synthetic planets via gravity synthesis. The assumptions we made during these modeling steps have implications for the results of the inference and should be carefully considered. For instance, we assumed the planetary region beneath the modeled lithosphere (D_l = 150 km) to have laterally uniform density distributions. However, as discussed earlier, this assumption is likely inaccurate, for instance due to the presence of a large mantle plume beneath the Elysium Planitia region. Root et al. (2026) found that the low degrees of the gravity spectrum are dominated by dynamic mantle flow, which explains the mismatch between the degree variance spectra in the training data set and the gravimetry data from Mars at low SH degrees (Figure 7). In a preliminary study, discussed in Supporting Information S1, we found that excluding the low SH degrees of $n \leq 12$ led to an even better agreement between the input and the degree variance spectra corresponding to the samples from the posterior distribution. However, this change resulted in inferior volume reduction, with 0.38% and 1.52% of the prior space contained within the 68% and 95% confidence intervals of the posterior distribution. This indicates significantly lower information gain. This leads to the conclusion that the planetary models should be improved in future studies to incorporate known deep mantle features in order to provide better constraints on the Matérn parameters.

A number of model parameters were assigned pre-set values based on findings of previous studies, although no clear consensus exists regarding these values. Therefore, it is important to understand the sensitivity of the analysis to these parameters and the potential impact of inaccurate planetary models. The main parameters controlling the flexure model, E and T_e, have little influence on the gravity spectrum, therefore, assumptions about these parameters are not expected to have a significant impact on the obtained Matérn parameters. Therefore, an imperfect removal of the flexure crust is unlikely to impact the accuracy of the results. However, future analyses might still benefit from including these parameters in the inference for a more comprehensive analysis, revealing potential hidden correlations between planetary variables. In addition, the density fluctuations

21699100, 2026, 7, Downloaded from https://agupubs.onlinelibrary.wiley.com/doi/10.1029/2026JE009757 by Technical University Delft, Wiley Online Library on [30/07/2026]. See the Terms and Conditions (https://onlinelibrary.wiley.com/terms-and-conditions) on Wiley Online Library for rules of use; OA articles are governed by the applicable Creative Commons License

were only modeled for a relatively thin region of the mantle. As it was shown in Figure 3, the value of D_l has a visible impact on the degree variance spectrum of gravity, and the chosen value will likely impact the inference results. It is likely that a lower assumed D_l results in larger estimated amplitudes in the lateral density distribution in the mantle, encoded mainly in the σ_m parameter. It is also important to interpret the inferred κ_m and ϵ_m parameters as an average value for the region below D_c and above D_m only. They do not provide information about the deeper mantle regions.

Recent findings from the analysis of Insight seismic data (Knapmeyer-Endrun et al., 2021) suggest that there are at least three separate crustal layers with different average densities and structure, which suggests that the one-layer crustal model adopted in this work is overly simplistic. The inferred crustal density characteristics can be interpreted as a weighted average across all crustal layers. Since surface gravity is most sensitive to the uppermost layer, the inferred values primarily reflect upper crustal properties. However, we need to be careful when interpreting the inferred values as corresponding to individual crustal layers. Density anomalies across layers are likely spatially correlated, though non-overlapping features can also be expected. For instance, a cone-like feature that widens with depth could produce larger, less fragmented features in the gravity data and broaden the inferred κ_c values. The inferred σ_c parameter is also likely overestimated, as it represents a weighted vertical average of variations between columns of density across crustal layers, resulting a broader range of possible values. Additionally, we did not separate the density of the topography from that of the crust, although, more realistically, they should be treated independently. The topographic densities may differ from those of the crust due to surface deposition from volcanic activity or sedimentation (Tanaka et al., 2014). A visual comparison between the crustal density distributions (Figure 9) and Martian topography (Figure 1a) reveals similarities in the small-scale textures and the presence of larger connected regions. While the obtained distributions could realistically represent the crustal structure, they are likely affected by the topography. By averaging the densities of the topography and the crust, we may obtain an inflated σ_c parameter compared to the true crustal value. This assumption can also affect the inferred ϵ_c and κ_c values. For instance, heavy cratering can lower κ_c by introducing small-scale near-surface structures with different densities. Overall, due to the relatively simple nature of the planetary models, further experiments are recommended that implement more detailed layer structure informed by for example, recent seismic findings. In addition, the obtained results are limited by the resolution, which only allows the modeling of features with the minimum size of 236 × 236 km corresponding to 4° × 4°. The analysis of higher-resolution gravity data would be required to resolve smaller κ and ϵ values. Building higher-resolution planetary models and analyzing gravity spectra up to the observable limit (∼95°), and even constraining our models further using Kaula's rule power-law estimates at higher degrees, is a highly desirable avenue for future research.

Finally, it is important to note, that the approximated posterior PDFs obtained from the NF inference should not be regarded as the mathematically "true" posteriors. While these were demonstrated to be consistent and informative, better results may be achievable with more effective training or network architecture. Therefore, these distributions represent the best current constraints on the inferred Matérn parameters, and future work could aim to achieve tighter distributions with reduced uncertainties. In this work, we implemented a physics-informed machine learning technique through the construction of a physics-based training data set, incorporating isostatic theory, statistical constraints using physically viable covariance functions, and the mathematical formulation of the gravitational fields of layered planets. Other machine learning approaches could be applied to the same problem and achieve similar or superior results, such as generative adversarial networks (GANs) (Goodfellow et al., 2014). Physics-informed machine learning can also take other forms when applied to gravity inverse problems, such as physics-informed neural networks (PINNs) (Raissi et al., 2019), where the physical laws governing planetary interiors could be incorporated directly into the loss function.

The obtained posterior probability distributions of the Matérn parameters are significantly constrained compared to our prior knowledge, as only 0.09% of the prior volume is contained within the 1σ confidence interval of the posterior PDF. The results indicate that the crust contains small-scale structures, while the mantle has smoother distributions with more gradual variations. A smooth distribution in the mantle is advantageous for local studies, as gravity anomalies on a small spatial scale are likely to originate from the crust, and the mantle does not need to be accounted for. It was also shown that both layers feature large-scale structures with correlated densities, with the crust and mantle densities constrained to 3042^{+93}_{-98} kg/m^3 and 3544^{+304}_{-221} kg/m^3, respectively. The obtained lateral density distributions for the mantle, visualized in Figure 9b, are indicative of the presence of global convection (Root et al., 2026).

21699100, 2026, 7, Downloaded from https://agupubs.onlinelibrary.wiley.com/doi/10.1029/2026JE009757 by Technical University Delft, Wiley Online Library on [30/07/2026]. See the Terms and Conditions (https://onlinelibrary.wiley.com/terms-and-conditions) on Wiley Online Library for rules of use; OA articles are governed by the applicable Creative Commons License

While the density range is not significantly constrained for the mantle, the more confident crustal estimates are consistent with previous studies, providing new evidence to support these findings. In some of the potential lateral density distributions visualized in Figure 9a, we can observe a dichotomy of density in the crust, which is supported by the seismic study by M. A. Wieczorek et al. (2022) using Insight measurements. Our assumed value of $D_c = 60$ km lies within the range of crustal thickness values permitted by M. A. Wieczorek et al. (2022) (30–72 km). For the crustal thickness maps most consistent with our model output (Figure 1b), they predict a low-density dichotomy between the highlands and lowlands, with a maximum difference of 100 kg/m^3 between the average densities. While their average crustal densities are slightly lower than those assumed in this study ($\bar{\rho}_c = 3{,}050$ kg/m^3), with 2,900 kg/m^3 for the highlands and 2,800–2,900 kg/m^3 for the lowlands, our assumption still lies below their maximum permissible value of 3,100 kg/m^3. Since this study does not aim to predict specific spatial maps of lateral density distributions, it is not possible to provide a direct estimate of the density dichotomy between the mean values of the highlands and lowlands. However, we can state that the predicted most likely standard deviation of $\sigma_c = 84$ kg/m^3 is consistent with the findings of M. A. Wieczorek et al. (2022). Lateral crustal density maps previously obtained from gravity data by Goossens et al. (2017) yield lower average crustal densities than the common values adopted in other studies, including this one. Their inferred lateral crustal density map also differs from ours as it spans a much wider range of densities (1,800–3,200 kg/m^3). However, it also features large, connected regions of density that are not strictly aligned with the dichotomy boundary, similar some of the maps shown in Figure 1b.

Besides directly using these results to study the densities in the Martian lithosphere, the posterior PDFs are also well suited to inform future analyses and gravity inversion attempts. The posterior distribution encodes all the information about the Matérn parameters of the density distributions in the crust and mantle contained within the gravitational degree variance spectrum between the 7th and 45th SH degrees. Since sampling from the NF is nearly instantaneous, the posterior PDF can be sampled efficiently, and these samples can be used as input for further analyses. These results may find applications in gravity inversions aimed at producing a global map of lithospheric densities, or they can be combined with other geophysical data to gain further insights about Mars's interior. Such approaches could also incorporate local information, for example, from the Elysium region, to constrain global density maps. The developed method can also be applied to other planets with relative ease by adjusting the prior conditions and planetary models.

9. Conclusion

The presented NF-based machine-learning technique makes it possible to decouple the statistical characteristics of the crustal and mantle density distributions using gravity observations. We find that the maximum-likelihood standard deviation of crustal density on Mars is ∼84 kg/m^3, while that of the mantle density down to 150 km depth is ∼70 kg/m^3. Our results indicate that the crust has density variations over small spatial scales, whereas the mantle has a relatively smooth density distribution and both layers contain large-scale connected features. The inferred density ranges are consistent with previous studies, and the characteristics of the density distributions agree with expected features of the Martian interior, such as ongoing global mantle convection and the presence of a crustal dichotomy. Therefore, this study provides constraints on Martian lithospheric densities using a statistical analysis technique consistent with previous literature. The results are expressed as a multivariate probability distribution of parameters describing the density structure of Mars, as encoded in the gravity spectrum within the SH degree range $7 < n < 45$. An advantage of this technique is that the posterior distribution can be efficiently and cheaply sampled, enabling its application in future studies aiming to produce multi-layered density maps of the Martian lithosphere.

Abbreviation

CDF	Cumulative distribution function
GSHA	Global spherical harmonic analysis
GSHS	Global spherical harmonic synthesis
NF	Normalizing Flow
PDF	Probability distribution function

RealNVP	Real-valued non-volume preserving
SD	Standard deviation
SH	Spherical harmonic

Conflict of Interest

The authors declare no conflicts of interest relevant to this study.

Availability Statement

The open-access software can be accessed via Zenodo (Rakoczi, 2026). The input data is publicly available on the PDS Geosciences Node (G. Neumann et al., 2003; M. Zuber et al., 2010).

Acknowledgments
This work was primarily supported by UK Research and Innovation (Grant ST/V005499/1). H. Rakoczi would like to thank the Planetary Exploration group at TU Delft for hosting her visit, which made this research and manuscript possible.

References

Airy, G. B. (1855). III. On the computation of the effect of the attraction of mountain-masses, as disturbing the apparent astronomical latitude of stations in geodetic surveys. *Philosophical Transactions of the Royal Society*, *145*, 101–104. https://doi.org/10.1098/rstl.1855.0003

Bayes, T. (1763). An essay towards solving a problem in the doctrine of chances. *Philosophical Transactions*, *53*, 370–418.

Belleguic, V., Lognonné, P., & Wieczorek, M. (2005). Constraints on the Martian lithosphere from gravity and topography data. *Journal of Geophysical Research*, *110*(E11), E11005. https://doi.org/10.1029/2005JE002437

Beuthe, M., Le Maistre, S., Rosenblatt, P., Pätzold, M., & Dehant, V. (2012). Density and lithospheric thickness of the THARSIS province from MEX Mars and MRO gravity data. *Journal of Geophysical Research*, *117*(E4). https://doi.org/10.1029/2011JE003976

Bozdag, E., Ruan, Y., Metthez, N., Khan, A., Leng, K., Wieczorek, M., et al. (2017). Simulations of seismic wave propagation on Mars. *Space Science Reviews*, *211*(1–4), 571–594. https://doi.org/10.1007/s11214-017-0350-z

Broquet, A., & Andrews-Hanna, J. (2022). Geophysical evidence for an active mantle plume underneath Elysium Planitia on Mars. *Nature Astronomy*, *7*, 1–10. https://doi.org/10.1038/s41550-022-01836-3

Cook, S. R., Gelman, A., & Rubin, D. B. (2006). Validation of software for Bayesian models using posterior quantiles. *Journal of Computational & Graphical Statistics*, *15*(3), 675–692. https://doi.org/10.1198/106186006X136976

Coulson, I., Beech, M., & Nie, W. (2007). Physical properties of Martian meteorites: Porosity and density measurements. *Meteoritics & Planetary Science*, *42*(12), 2043–2054. https://doi.org/10.1111/j.1945-5100.2007.tb01006.x

Dinh, L., Sohl-Dickstein, J., & Bengio, S. (2017). Density estimation using real NVP. https://doi.org/10.48550/arXiv.1605.08803

Drilleau, M., Beucler, r., Shi, J., Knapmeyer-Endrun, B., Garcia, R. F., Ansan, V., et al. (2023). Structure of the Martian crust below insight from surface waves and body waves generated by nearby meteoroid impacts. *Geophysical Research Letters*, *50*(23), e2023GL104601. https://doi.org/10.1029/2023GL104601

Drilleau, M., Samuel, H., Garcia, R. F., Rivoldini, A., Perrin, C., Wieczorek, M., et al. (2024). Constraints on lateral variations of Martian crustal thickness from seismological and gravity field measurements. *Geophysical Research Letters*, *51*(4), e2023GL105701. https://doi.org/10.1029/2023GL105701

Durkan, C., Bekasov, A., Murray, I., & Papamakarios, G. (2020). nflows: Normalizing flows in PyTorch. *Zenodo*. https://doi.org/10.5281/zenodo.4296287

Ermakov, A. I., Park, R. S., & Bills, B. G. (2018). Power laws of topography and gravity spectra of the solar system bodies. *Journal of Geophysical Research: Planets*, *123*(8), 2038–2064. https://doi.org/10.1029/2018JE005562

Genova, A., Goossens, S., Lemoine, F. G., Mazarico, E., Neumann, G. A., Smith, D. E., & Zuber, M. T. (2016). Seasonal and static gravity field of Mars from MGS, Mars Odyssey and MRO radio science. *Icarus*, *272*, 228–245. https://doi.org/10.1016/j.icarus.2016.02.050

Gneiting, T. (2013). Strictly and non-strictly positive definite functions on spheres. *Bernoulli*, *19*(4), 1327–1349. https://doi.org/10.3150/12-BEJSP06

Gneiting, T., Kleiber, W., & Schlather, M. (2010). Matern cross-covariance functions for multivariate random fields. https://doi.org/10.1198/jasa.2010.tm09420

Goodfellow, I. J., Pouget-Abadie, J., Mirza, M., Xu, B., Warde-Farley, D., Ozair, S., et al. (2014). Generative adversarial networks. arXiv: 1406.2661.

Goossens, S., Sabaka, T. J., Genova, A., Mazarico, E., Nicholas, J. B., & Neumann, G. A. (2017). Evidence for a low bulk crustal density for Mars from gravity and topography. *Geophysical Research Letters*, *44*(15), 7686–7694. https://doi.org/10.1002/2017GL074172

Grott, M., & Breuer, D. (2008). The evolution of the Martian elastic lithosphere and implications for crustal and mantle rheology. *Icarus*, *193*(2), 503–515. https://doi.org/10.1016/j.icarus.2007.08.015

Guinard, A., Fienga, A., Mémin, A., & Ganino, C. (2025). Coupled tidal tomography and thermal constraints for probing Mars viscosity profile. *Icarus*, *425*, 116318. https://doi.org/10.1016/j.icarus.2024.116318

Guinness, J., & Fuentes, M. (2015). Isotropic covariance functions on spheres: Some properties and modeling considerations. *Journal of Multivariate Analysis*, *143*, 143–152. https://doi.org/10.1016/j.jmva.2015.08.018

Kaula, W. M. (1963). Determination of the Earth's gravitational field. *Reviews of Geophysics*, *1*(4), 507–551. https://doi.org/10.1029/RG001i004p00507

Kaula, W. M. (1966). *Theory of satellite geodesy: Applications of satellites to geodesy*. Blaisdell Publishing Company. Retrieved from https://archive.org/details/theoryofsatellit0000kaul

Khan, A., Ceylan, S., van Driel, M., Giardini, D., Lognonné, P., Samuel, H., et al. (2021). Upper mantle structure of Mars from InSight seismic data. *Science*, *373*(6553), 434–438. https://doi.org/10.1126/science.abf2966

Kim, D., Duran, C., Giardini, D., Plesa, A.-C., Stähler, S. C., Boehm, C., et al. (2023). Global crustal thickness revealed by surface waves orbiting Mars. *Geophysical Research Letters*, *50*(12), e2023GL103482. https://doi.org/10.1029/2023GL103482

21699100, 2026, 7, Downloaded from https://agupubs.onlinelibrary.wiley.com/doi/10.1029/2026JE009757 by Technical University Delft, Wiley Online Library on [30/07/2026]. See the Terms and Conditions (https://onlinelibrary.wiley.com/terms-and-conditions) on Wiley Online Library for rules of use; OA articles are governed by the applicable Creative Commons License

Kingma, D. P., & Ba, J. (2017). Adam: A method for stochastic optimization. https://doi.org/10.48550/arXiv.1412.6980
Knapmeyer-Endrun, B., Panning, M. P., Bissig, F., Joshi, R., Khan, A., Kim, D., et al. (2021). Thickness and structure of the Martian crust from insight seismic data. *Science*, *373*(6553), 438–443. https://doi.org/10.1126/science.abf8966
Kobyzev, I., Prince, S. J., & Brubaker, M. A. (2021). Normalizing flows: An introduction and review of current methods. *IEEE Transactions on Pattern Analysis and Machine Intelligence*, *43*(11), 3964–3979. https://doi.org/10.1109/tpami.2020.2992934
Konopliv, A. S., Park, R. S., & Folkner, W. M. (2016). An improved JPL Mars gravity field and orientation from Mars orbiter and lander tracking data. *Icarus*, *274*, 253–260. https://doi.org/10.1016/j.icarus.2016.02.052
Kraus, H. (1967). *Thin elastic shells; an introduction to the theoretical foundations and the analysis of their static and dynamic behavior*. Wiley. Retrieved from https://www.worldcat.org/isbn/0471507202
Liang, F., Yan, J., Zhao, J., higuo, M., & Barriot, J.-P. (2022). Searching for buried craters on Mars based on gravity potential field separation method. *Planetary and Space Science*, *220*, 105532. https://doi.org/10.1016/j.pss.2022.105532
McGovern, P. J., Solomon, S. C., Smith, D. E., Zuber, M. T., Simons, M., Wieczorek, M. A., et al. (2004). Correction to "localized gravity/topography admittance and correlation spectra on Mars: Implications for regional and global evolution". *Journal of Geophysical Research*, *109*(E7). https://doi.org/10.1029/2004JE002286
Mittelholz, A., Johnson, C. L., Fillingim, M., Grimm, R. E., Joy, S., Thorne, S. N., & Banerdt, W. B. (2023). Mars' external magnetic field as seen from the surface with insight. *Journal of Geophysical Research: Planets*, *128*(1), e2022JE007616. https://doi.org/10.1029/2022JE007616
Mussini, J. (2019). *An anisotropic fexural isostasy method for investigating the Martian lithosphere* (Master's thesis). Delft University of Technology. Retrieved from http://resolver.tudelft.nl/uuid:5d77cc6e-a4c5-433e-b898-d5e8b9f4d58d
Neumann, G., Zuber, M., & Smith, D. E. (2003). *MOLA mission experiment gridded data record*. NASA Planetary Data System. https://doi.org/10.17189/1519460
Neumann, G. A., Zuber, M. T., Wieczorek, M. A., McGovern, P. J., Lemoine, F. G., & Smith, D. E. (2004). Crustal structure of Mars from gravity and topography. *Journal of Geophysical Research*, *109*(E8). https://doi.org/10.1029/2004JE002262
Nimmo, F., & Stevenson, D. J. (2001). Estimates of Martian crustal thickness from viscous relaxation of topography. *Journal of Geophysical Research*, *106*(E3), 5085–5098. https://doi.org/10.1029/2000JE001331
Papamakarios, G., Nalisnick, E., Rezende, D. J., Mohamed, S., & Lakshminarayanan, B. (2021). Normalizing flows for probabilistic modeling and inference. *Journal of Machine Learning Research*, *22*(57), 1–64. Retrieved from https://jmlr.org/papers/v22/19-1028.html
Paszke, A., Gross, S., Massa, F., Lerer, A., Bradbury, J., Chanan, G., et al. (2019). Pytorch: An imperative style, high-performance deep learning library. In *Advances in neural information processing systems 32* (pp. 8024–8035). Curran Associates, Inc. https://doi.org/10.48550/arXiv.1912.01703
Pauer, M., & Breuer, D. (2008). Constraints on the maximum crustal density from gravity–topography modeling: Applications to the southern highlands of Mars. *Earth and Planetary Science Letters*, *276*(3), 253–261. https://doi.org/10.1016/j.epsl.2008.09.014
Phillips, R. J., Saunders, R. S., & Conel, J. E. (1973). Mars: Crustal structure inferred from Bouguer gravity anomalies. *Journal of Geophysical Research*, *78*(23), 4815–4820. https://doi.org/10.1029/JB078i023p04815
Phillips, R. J., Zuber, M. T., Solomon, S. C., Golombek, M. P., Jakosky, B. M., Banerdt, W. B., et al. (2001). Ancient geodynamics and global-scale hydrology on Mars. *Science*, *291*(5513), 2587–2591. https://doi.org/10.1126/science.1058701
Plesa, A.-C., Padovan, S., Tosi, N., Breuer, D., Grott, M., Wieczorek, M. A., et al. (2018). The thermal state and interior structure of Mars. *Geophysical Research Letters*, *45*(22), 12198–12209. https://doi.org/10.1029/2018GL080728
Raissi, M., Perdikaris, P., & Karniadakis, G. (2019). Physics-informed neural networks: A deep learning framework for solving forward and inverse problems involving nonlinear partial differential equations. *Journal of Computational Physics*, *378*, 686–707. https://doi.org/10.1016/j.jcp.2018.10.045
Rakoczi, H. (2026). Marsinf. *Zenodo*. https://doi.org/10.5281/zenodo.18495086
Rezende, D. J., & Mohamed, S. (2016). Variational inference with normalizing flows. https://doi.org/10.48550/arXiv.1505.05770
Root, B. C. (2021). GSH is a Matlab package to do global spherical harmonic analyses (GSHA) and synthesis (GSHS) for crust1.0. 4TU. *ResearchData*. https://doi.org/10.4121/16764238.V1
Root, B. C., Novák, P., Dirkx, D., Kaban, M., Van der Wal, W., & Vermeersen, L. (2016). On a spectral method for forward gravity field modelling. *Journal of Geodynamics*, *97*, 22–30. https://doi.org/10.1016/j.jog.2016.02.008
Root, B. C., Qin, W., van der Tang, Y., & Thieulot, C. (2026). Describing the global gravity field of Mars with lithospheric flexure and deep mantle flow. *Journal of Geophysical Research: Planets*, *131*(2), e2024JE008765. https://doi.org/10.1029/2024JE008765
Samuel, H., Drilleau, M., Rivoldini, A., Xu, Z., Huang, Q., Garcia, R., et al. (2023). Geophysical evidence for an enriched molten silicate layer above Mars's core. *Nature*, *622*(7984), 712–717. https://doi.org/10.1038/s41586-023-06601-8
Shi, J., Plasman, M., Knapmeyer-Endrun, B., Xu, Z., Kawamura, T., Lognonné, P., et al. (2023). High-frequency receiver functions with event S1222a reveal a discontinuity in the Martian shallow crust. *Geophysical Research Letters*, *50*(5), e2022GL101627. https://doi.org/10.1029/2022GL101627
Smith, D. E., Zuber, M. T., Frey, H. V., Garvin, J. B., Head, J. W., Muhleman, D. O., et al. (2001). Mars orbiter laser altimeter: Experiment summary after the first year of global mapping of Mars. *Journal of Geophysical Research*, *106*(E10), 23689–23722. https://doi.org/10.1029/2000JE001364
Stähler, S. C., Khan, A., Banerdt, W. B., Lognonné, P., Giardini, D., Ceylan, S., et al. (2021). Seismic detection of the Martian core. *Science*, *373*(6553), 443–448. https://doi.org/10.1126/science.abi7730
Talts, S., Betancourt, M., Simpson, D., Vehtari, A., & Gelman, A. (2020). Validating Bayesian inference algorithms with simulation-based calibration. https://doi.org/10.48550/arXiv.1804.06788
Tanaka, K. L., Skinner, J. J. A., Dohm, J. M., Irwin, I. R. P., Kolb, E. J., Fortezzo, C. M., et al. (2014). Geologic map of Mars [Scientific Investigations Map 3292]. https://doi.org/10.3133/sim3292
Taylor, N., Johnson, J., Herd, R., & Regan, C. (2020). What can Olympus mons tell us about the Martian lithosphere? *Journal of Volcanology and Geothermal Research*, *402*, 106981. https://doi.org/10.1016/j.jvolgeores.2020.106981
Turcotte, D. L., Shcherbakov, R., Malamud, B. D., & Kucinskas, A. B. (2002). Is the Martian crust also the Martian elastic lithosphere? *Journal of Geophysical Research*, *107*(E11), 1-1–20. https://doi.org/10.1029/2001JE001594
van Brummen, B. (2022). *Mars gravity inversion: Investigating the lateral density variations of the Martian lithosphere* Master's thesis. Delft University of Technology. Retrieved from https://resolver.tudelft.nl/uuid:1f8beaf8-a97a-47d5-a57b-38b91a35bec9
Watts, A. B. (2023). *Isostasy and flexure of the lithosphere* (2nd ed.). Cambridge University Press. https://doi.org/10.1017/9781139027748
Wieczorek, M. (2015). Gravity and topography of the terrestrial planets. In *Treatise on geophysics* (2nd ed., pp. 153–193). Elsevier. https://doi.org/10.1016/B978-0-444-53802-4.00169-X

21699100, 2026, 7, Downloaded from https://agupubs.onlinelibrary.wiley.com/doi/10.1029/2026JE009757 by Technical University Delft, Wiley Online Library on [30/07/2026]. See the Terms and Conditions (https://onlinelibrary.wiley.com/terms-and-conditions) on Wiley Online Library for rules of use; OA articles are governed by the applicable Creative Commons License

Wieczorek, M. A., Broquet, A., McLennan, S. M., Rivoldini, A., Golombek, M., Antonangeli, D., et al. (2022). Insight constraints on the global character of the Martian crust. *Journal of Geophysical Research: Planets*, *127*(5), e2022JE007298. https://doi.org/10.1029/2022JE007298

Wieczorek, M. A., & Zuber, M. T. (2004). Thickness of the Martian crust: Improved constraints from geoid-to-topography ratios. *Journal of Geophysical Research*, *109*(E1). https://doi.org/10.1029/2003JE002153

Williams, M. J., jmcginn, federicostak, & Veitch, J. (2023). uofgravity/glasflow: v0.2.0. *Zenodo*. https://doi.org/10.5281/zenodo.7598678

Zuber, M., Konopliv, A., & Lemoine, F. G. (2010). MRO radio science derived gravity science data products v1.0. *NASA Planetary Data System*. https://doi.org/10.17189/1519521

Zuber, M. T., Solomon, S. C., Phillips, R. J., Smith, D. E., Tyler, G. L., Aharonson, O., et al. (2000). Internal structure and early thermal evolution of Mars from Mars global surveyor topography and gravity. *Science*, *287*(5459), 1788–1793. https://doi.org/10.1126/science.287.5459.1788

21699100, 2026, 7, Downloaded from https://agupubs.onlinelibrary.wiley.com/doi/10.1029/2026JE009757 by Technical University Delft, Wiley Online Library on [30/07/2026]. See the Terms and Conditions (https://onlinelibrary.wiley.com/terms-and-conditions) on Wiley Online Library for rules of use; OA articles are governed by the applicable Creative Commons License